



UNIVERSITÀ DEGLI STUDI DI PADOVA

Dipartimento di Fisica e Astronomia “Galileo Galilei”

Corso di Laurea Magistrale in Astrophysics and Cosmology

Tesi Magistrale

Photometry and proper motions of Milky-Way satellites with
the Hubble Space Telescope

Relatore

Prof. Antonino P. Milone

Correlatori

Dott. Emanuele Dondoglio

Dott. Giacomo Cordoni

Laureando

Andrea Troia

Anno Accademico 2022/2023

Contents

1 Introduction	5
1.1 Dwarf galaxies	5
1.2 Dwarf galaxies in the Local Group	9
1.2.1 Stars in a Dwarf Galaxy	10
1.3 Ultra faint dwarf galaxies	10
1.3.1 Stellar kinematics and metallicities	14
1.3.2 Star formation Histories	17
1.3.3 Dark Matter	17
1.4 Bootes I	18
1.5 Outline and purpose of the Thesis	26
2 Data and Data reduction	27
2.1 Instrumentation	27
2.1.1 Hubble Space Telescope	27
2.1.2 GAIA	28
2.2 Dataset	28
2.2.1 Effective Point Spread Function	28
2.2.2 Deriving the effective PSF Model for Bootes I	29
2.3 Catalog building	31
2.4 Star Analysis	31
2.5 Study of the proper motion	34
2.5.1 Proper motion techniques	34
2.5.2 Proper motion Analysis	36
2.6 Calibration	38
3 Data Analysis	41
3.1 HST Color Magnitude Diagram and relative proper motion.	41
3.2 GAIA CMD	42
3.3 Bootes I Orbit	52
4 Discussion and conclusions	55

Abstract

This thesis proposes a new method to estimate the absolute proper motion of the ultra-faint dwarf galaxy (UFD) Bootes I. While previous proper-motion determinations were based either on background galaxies and quasars or on the GAIA absolute motions of UFD stars alone, here, I propose a novel approach to derive improved proper motions, by combining relative proper motions from multi-epoch Hubble Space Telescope (HST) images and absolute proper motions of both UFD members and field stars from GAIA Early Data Release 3 (eDR3).

The thesis provides a short review of dwarf galaxies, and in particular of UFDs, which are low-luminosity galaxies dominated by dark matter. By exploiting multi-epoch images collected with the Wide Field Channel of the Advanced Camera for Surveys on board HST, I was able to derive high-precision photometry and astrometry of stars in the direction of Bootes I. Moreover, I derived accurate stellar proper motions relative to Bootes I, and used them to separate the bulk of Bootes I members from field stars. The absolute proper motion of the UFD is then derived by combining the relative proper motions from HST and the absolute GAIA eDR3 proper motions for the stars in common between the two astro-photometric datasets. I show that our new method provides improved proper motion determinations when compared to results obtained with traditional methods and by using proper motions from GAIA eDR3 Bootes I stars in the same field of view.

As a byproduct of this work, I derived for the first time, the color-magnitude diagram (CMD) of proper-motion selected Bootes I stars. This diagram is used to infer the main parameters of this UFD, including metallicity, age, reddening, and distance by means of isochrone fitting. Finally, by combining the 6-dimensional information on the position, i.e. right ascension, declination and distance, and motion, i.e. proper motions and radial velocity, I determined the orbit of Bootes I and its orbital properties

Chapter 1

Introduction

In this chapter, I present the modern view of dwarf galaxies and their classification. I will focus on ultra-faint dwarf galaxies (UFDs) and the most recent discoveries on these enigmatic objects. I finally summarise the impact of studies on the UFDs to constrain the formation and evolution of the Galaxy and shed light on the dark matter.

This chapter is organized as follows. In Section 1.1, I will summarize the properties of dwarf galaxies in the Local Group and in the distant universe, illustrate their main properties, and the different typologies in which they can be subdivided. In particular, I will focus on dwarf spheroids and irregular dwarfs. Section 1.2 is dedicated to the ultra-faint dwarf galaxies. I first review the distinctive characteristics of the UFDs and discuss the differences with the other sub-classes of galaxies. Then, I will show the main method to identify UFDs and discuss their stellar kinematics, metallicities, and star formation histories, finally, I will investigate the dark matter content of UFDs. Section 1.3 is focused on Bootes I, which is the UFD studied in this thesis and summarizes the main results from the papers of [Brown et al. \(2014\)](#) and [Koposov et al. \(2018\)](#)

1.1 Dwarf galaxies

The past definitions of dwarf galaxies are based on size ([Hodge \(1971\)](#)) and the presence of a dark matter halo ([Mateo \(1998\)](#)). So what differentiates dwarfs from bigger galaxies is classically considered to be the amount of retained baryonic matter. In general, large late-type galaxies sit on the constant central surface brightness ridge defined by [Freeman \(1970\)](#) and appear to have managed to retain most of their initial baryons composition. On the other hand, for galaxies below this limit, it seems that the fainter they are, the higher the fraction of baryons they have lost. This could be due to Supernova winds and/or tidal interactions, which are effective when a galaxy lacks a suitably deep potential well to be able to hold onto to its gas and/or metals. The galaxies above this central surface brightness limit are either currently forming stars very actively, such as blue compact dwarfs (BCDs), or they were very active star formation activity in the past. The definition of a galaxy based on the presence of a dark matter halo excludes globular clusters, which are believed not to contain any dark matter, and tidal dwarfs which are

a different category of objects that formed much later than the epoch of galaxy formation.

In modern times, the idea that dwarf galaxies are in any way special systems is left behind. Many galactic properties (e.g., potential well, metallicity, size) correlate with mass and luminosity, and all types of galaxies show continuous relations in structural, kinematic, and population features between the biggest and the smallest of their kind. The only justification for segregating dwarf galaxies from other types is to study specific aspects of galaxy formation and evolution on a small scale.

The taxonomy of dwarf galaxies typically is a controversial field. As illustrated in Figure 1.1, all galaxies that are fainter than $M_B \leq -16$ ($M_V \leq -17$) and more spatially extended than globular clusters are dwarf galaxies (Tammann (1994)). This is broadly consistent with the presence of a mass threshold, where the outflows tend to affect the baryonic mass of a galaxy significantly. This includes a number of different types:

- **Dwarf spheroids** (dSphs) are characterized by low luminosity and lack of gas, so they are not forming stars anymore (similar to elliptical galaxies). They are defined as early-type objects. This kind of object is observed even in the local group. Due to the lack of gas, their internal kinematics can only be determined from stellar velocity dispersion. Their luminosities are so low that Ursa Minor, Carina, and Draco, the known dwarf spheroidal galaxies with the lowest luminosities, have mass-to-light ratios (M/L) greater than that of the Milky Way. They have typically not formed stars for at least several hundred million years (e.g., Fnx), and in several cases for much longer. Typical mass is around 10^7 Solar mass, and taking into consideration the Sagittarius dSphs have an apparent magnitude $M_V=4.5$ and are typically larger than one square degree in the sky. This kind of galaxy is typically associated with large galaxies like our own. They are extremely close to us, with the majority at distances < 130 kpcs.
- **Dwarf irregular** (dIrrs) are gas-rich and are characterized by star formation, so we can spot blue stars that are produced in a recent period, defined as late-type star-forming. Due to the presence of gas the internal kinematics can be easily determined from it, their distance makes them challenging targets to determine stellar velocities from RGB stars. Likewise, abundances in dIs are typically [O/H] measurements in young HII regions. They are a numerous and often fairly luminous class within the Local Group. They are typically at distances >400 kpcs. Leo A is one of the deepest (Cole et al. (2007)) and most accurate ever made for a dI.
- **Ultra-compact dwarf** (UCD) has been discovered recently in the core region of nearby galaxy clusters characterized by old stellar populations. Defined also as very-low surface brightness objects. They may be objects like ω Cen, which is now often considered to be the tidally stripped nucleus of a compact system. The structural properties of ω Cen and UCDs clearly overlap (see Figure 1.1). They have also been proposed to be low-luminosity ellipticals like M 32, but Figure 1.1 would tend to argue against this.

- **Ultra-faint dwarf** (UFD) are galaxies that contain from a few hundred to one hundred thousand stars are the most dark matter-dominated system, and their faintness makes them extremely hard objects to observe. They are identified as dwarf galaxies from spectra but are of similar compactness to globular clusters.

As has been stated throughout the years (Boselli et al. (2008)), and references therein), a morphological classification is only useful if it is paired with a physical understanding of the process involved, but at the moment this is not complete, hence, structural parameters and their relations may give us clues to the underlying physics. But when complex systems are studied we have to be careful to not over-interpret these global measures. This requires care to establish a meaningful comparison of the same properties of such different systems.

Figure 1.1 made by Kormendy (1985), illustrates how dwarfs compare with all other galaxies with no real evidence of a discontinuity, from a comparison of the absolute magnitude (M_V) and central surface brightness (μ_V) of galaxies (Figure 1.1A), the early- and late-type dwarfs appear to fall along similar relations, overlapping with BCDs and other larger late-type system as well as faint spiral galaxy disks and those galaxies defined as spheroidals by Boselli et al. (2008). This means systems that resemble late-type galaxies in their structural properties but are no longer forming stars. The ultra-faint dwarf galaxy is clearly separated but arguably follows the same relation as the other dwarfs.

In Figure 1.1B the varying physical size scales of different galaxy types and globular clusters are shown by plotting M_V against the half-light radius $r_{1/2}$ after Belokurov et al. (2007). In this plot, there is a clear trend for more luminous galaxies to be larger. The ellipticals clearly fall on a distinct narrow sequence. Dwarf galaxies, that is, BCDs, late-type and spheroidal galaxies fall along a similar, although offset, tilted, and more scattered relation to the elliptical galaxies. Also from Figure 1.1 it can be seen that there is no clear separation between dwarf galaxies and the larger late-type and spheroidal system. The dIs, BCDs, dSphs, hence late-type and spheroidal galaxies tend to overlap with each other in this parameter space. The overlapping properties of early- and late-type dwarfs have long been shown as convincing evidence that early-type dwarfs are the same as late-type system that has been stripped of their gas (Kormendy (1985)). This is quite different from the distinction between ellipticals and spirals, which show a more fundamental difference (Boselli et al. (2008)). There is no clear break that distinguishes a dwarf from a larger galaxy and, hence, the most simple definition does not have an obvious physical meaning, as recognized by Tammann (1994).

Whatever the precise definition of sub-classes, dwarf galaxies cover a large range of size, surface brightness, and distance, and so they are usually studied with different techniques with varying sensitivity to detail. Some galaxies are just easier to study than others. This distribution also leads to biases in understanding the full distribution of properties of a complete sample. It is not easy to compare the properties of dwarf galaxies that have ongoing star formation, with those that do not. Indeed, the properties that can be measured, and then compared, are often different from one type of galaxy to another.

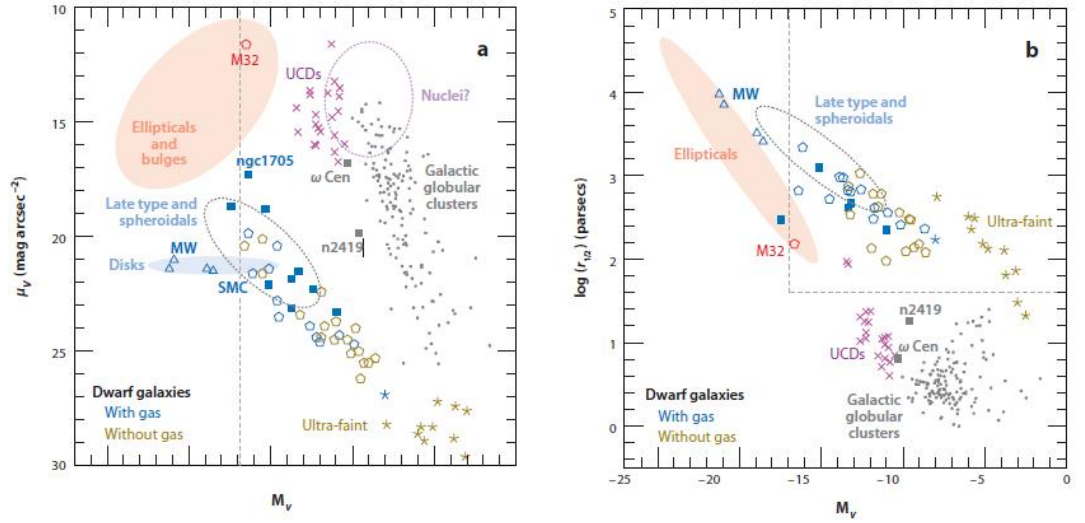


Figure 1.1: Relationships between structural properties for different types of galaxies, including as dotted lines the classical limits of the dwarf galaxy-class as defined by Tammann (1994)(a). The absolute magnitude, M_V , versus central surface brightness μ_V plane; (b) The M_V versus half-light radius $r_{1/2}$ plane. Marked with colored ellipses are the typical locations of elliptical galaxies and bulges (light red), spiral galaxy disks (light blue), galactic nuclei (dashed purple), and large early-(spheroidals) and late-type systems (dashed grey). The ultracompact dwarfs (UCDs) studied in the Virgo and Fornax clusters are marked with purple crosses. Local Group dwarf galaxies are plotted as open pentagons, blue for systems with gas, and yellow for systems without gas. The recently discovered ultrafaint dwarfs are given star symbols and the same color code.

1.2 Dwarf galaxies in the Local Group

The Local Group dwarf galaxies offer a unique window to the detailed properties of the most common type of galaxy in the Universe. The Local Group is an ordinary collection of dwarf galaxies dominated by two giant spirals. The dwarfs of the Local Group provide a uniquely well-studied and statistically useful sample of low-luminosity galaxies. Indeed, virtually all currently known dwarfs less luminous than $M_V \sim -11.0$ are found in the Local Group (Whiting et al. (1997)). Dwarf galaxies represent the dominant population, by number, of the present-day Universe (Marzke & da Costa (1997)), and they were almost certainly much more numerous in past epochs (Ellis (1997)). Studies of nearby clusters (Jones et al. (1998) and references therein) suggest that the summed optical luminosity of all dwarfs may rival that of the giant high-surface brightness galaxies in these environments. The total dwarf population of the Local Group at that time was 14 galaxies, including the Magellanic Clouds, with six additional uncertain cases. The actual number is 38. More dwarfs have been confirmed or identified as Local Group members in the past 27 years than during the previous 222 years beginning with Le Gentil's discovery of M32.

There are fundamental reasons why the dwarfs of the Local Group remain especially important:

- The Local Group contains a unique mixture of low-luminosity galaxies of both types that provide some ways to address this question.
- Low-luminosity dwarfs tend to be metal poor; thus, the low luminosity dwarfs in the Local Group represent a sample of galaxies that is still largely composed of nearly primordial material. Dwarf galaxy abundances are typically determined from their HII regions, but only in the Local Group can we also obtain reliable abundances from resolved stellar populations.
- Dwarfs are the simplest galactic systems known. However, Local Group dwarfs are plainly telling us that “simple” is a relative term. The star formation and chemical-enrichment histories of these galaxies are complex, varied, and in most cases triggered and sustained by as-yet unknown mechanisms.
- Dwarf galaxies may be among the darkest single galaxies known. They play an important role in addressing the DM problem, having already placed interesting constraints on the nature and distribution of DM, and even whether the DM paradigm is valid for these systems.
- There is considerable evidence of ongoing, past, and future interactions between Local Group dwarfs and larger galaxies, which may have helped assemble the larger Local Group galaxies over time. Recent measurements of the star-formation histories, space motions, three-dimensional shapes, and detailed internal kinematics of some of these interacting dwarfs in the Local Group offer new constraints on the dwarf/giant relationship and interaction models (Unavane et al. (1996)).

Galaxies in which the individual stars can be resolved are those that can be studied in the greatest detail, this provides the most accurate star formation histories (SFHs)

going back to the earliest times. Thus, dwarf galaxies provide an overview of galaxy evolution in miniature that will also be relevant to understanding the early years of their larger cousins and the important physical processes that govern star formation and its impact on the surrounding interstellar medium.

1.2.1 Stars in a Dwarf Galaxy

To study the life and the evolution of a dwarf galaxy is important to take into consideration the CMD Figure 1.3. By this, is clear the presence of at least one old population and a plume of Blue objects that are not only Blue straggler but the signature of a young stellar population, and so the presence of multiple stellar populations.

To compute the star formation rate the observed CMD is compared with a large number of simulated CMD of simple stellar population, where there is the best fit, in a specific region of the CMD, the age and metallicity can be retrieved by the isochrones. Another way to study the data is using a 3D plot considering the variation of metallicity as function of age and star formation rate with time Figure 1.4. The results for LGS-3 are that 80% of the star formed at redshift $Z > 1$ (before 8 Gyr old) this are similar to the spheroidal dwarf galaxies, there is a residual star formation after 9 Gyr and some star formation younger than 1 Gyr old.

1.3 Ultra faint dwarf galaxies

The dwarf galaxies known prior to 2005 have absolute magnitudes brighter than $M_V = -8.7$, corresponding to V-band luminosities larger than $2.5 * 10^5 L_\odot$. Their Plummer (half-light) radii are $\leq 200 pc$ and, except for Sextans and Ursa Minor, their central surface brightnesses are $< -26 \text{ mag arcsec}^{-2}$. In contrast, the dwarfs discovered in SDSS and other modern surveys are up to a factor of $\sim 1,000$ less luminous, with half-light radii as small as $\sim 20 pc$ and surface brightnesses that can be $\sim 2-3 \text{ mag arcsec}^{-2}$ fainter than that of Sextans.

The nature of these new satellites was not immediately clear. Over the next several years, spectroscopy of stars in these objects pointed strongly to the conclusion that they were dwarf galaxies rather than globular clusters (Simon & Geha (2007)). Given the clear differences in global properties relative to previously known dwarf galaxies, the community rapidly began referring to these objects as “ultra-faint” dwarfs, a term first used by Willman et al. (2005). However, no formal definition of such a class was ever offered in the literature, and the usage of it has not been entirely consistent. Despite this new nomenclature, it is now obvious that UFDs continuously extend the properties of more luminous dwarfs in stellar mass, surface brightness, size, dynamical mass, and metallicity (see Figure 1.5). They are not a physically distinct class of objects. Nevertheless, there are several reasons why it may be useful to refer to them via a separate label. In particular, UFDs represent the extreme end (we presume) of the distribution of galaxy properties, orders of magnitude beyond the previously known dwarfs in some respects.

Finally, it is tempting to suggest that UFDs might differ from classical dSphs in that their star formation was shut off by reionization at $z \geq 6$ instead of continuing to lower

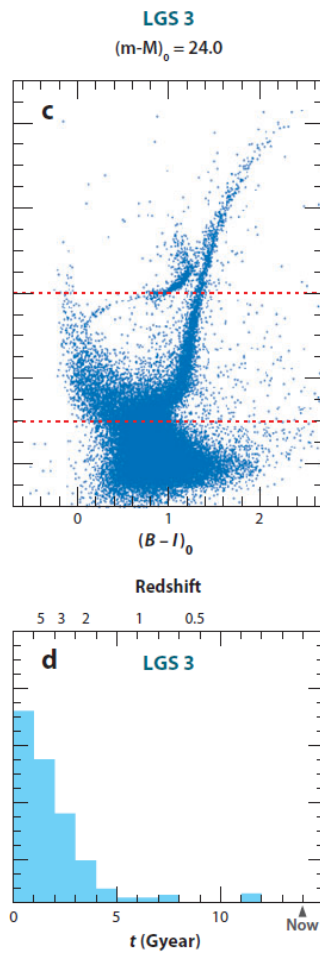


Figure 1.2: Hubble Space Telescope/Advanced Camera for Surveys (HST/ACS) color-magnitude diagrams (CMDs) and star-formation histories (SFHs). (c,d) LGS 3, a transition-type dwarf galaxy (S. Hildago & the LCID team, in preparation). These results come from the LCID project (Gallart et al. (2007), Cole et al. (2007)), which is a large program designed to exploit the exquisite image quality of the HST/ACS to obtain uniquely detailed CMDs going back to the oldest main sequence turn offs for a sample of dwarf galaxies. The SFHs come from synthetic CMD analysis and the ages are also shown in terms of redshift.

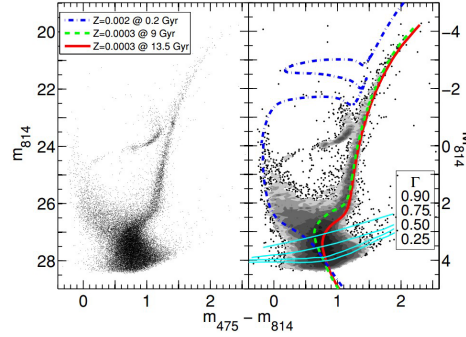


Figure 1.3: CMD LGS3 Dwarf galaxy by [Hidalgo et al. \(2011\)](#) Isochrones proved a first indicator of the star-formation history and the metallicity of the star populations.

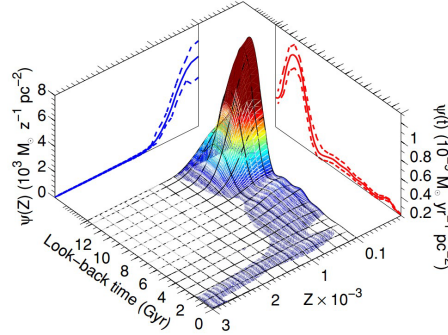


Figure 1.4: 3D CMD by Hidalgo et al(2011).

redshift. Although this hypothesis is consistent with the available data, the sample of $M_V - 9$ dwarf galaxies with precision star-formation histories is too small to draw firm conclusions yet. If this idea turns out to be correct, it would provide a physically motivated division between UFDs and classical dwarfs.

Based on the above discussion, we suggest that dwarf galaxies with absolute magnitudes fainter than $M_V = -7.7$ ($L = 10^5 L_\odot$) be considered UFDs. Among the post-2005 discoveries, only four galaxies are within 1 mag of this boundary: CVn I ($M_V = -8.7$), Crater II ($M_V = -8.2$), Leo T ($M_V = -8.0$), and Eridanus II ($M_V = -7.1$). The first three of these systems stand out from the fainter population in obvious ways: CVn I is substantially more luminous, larger, and more metal-rich ([Martin et al. \(2007\)](#), [Martin et al. \(2008\)](#); [Simon & Geha \(2007\)](#), [Muñoz et al. \(2018\)](#)); Crater II is a factor of ~ 4 more extended than any fainter dwarf ([Torrealba et al. \(2016\)](#)); and Leo T hosts neutral gas and recent star formation ([de Jong et al. \(2008\)](#), [Ryan-Weber et al. \(2008\)](#)).

This object could respond to one of the primary quests of astronomy which concern the formation of structure in the universe. The Λ cold dark matter cosmological model

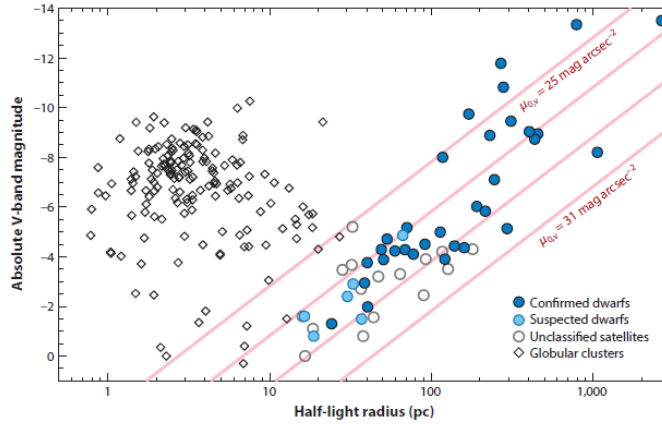


Figure 1.5: Distribution of Milky Way satellites in absolute magnitude M_V and half-light radius. Confirmed dwarf galaxies are displayed as dark blue filled circles, and objects suspected to be dwarf galaxies but for which the available data are not conclusive are shown as cyan filled circles. Dwarf galaxy candidates without any published classification (usually because of the lack of spectroscopy) are shown as open grey circles. The faint candidates with $R_{1/2} \geq 50 pc$ are almost certainly dwarf galaxies, but we do not include them in the confirmed category here given the currently available observations. The open black diamonds represent the Milky Way's globular clusters. Lines of constant central surface brightness (at 25, 27, 29, and 31 mag arcsec $^{-2}$ in V band) are plotted in pink.

For stellar systems brighter than $M_V = -5$ there is no ambiguity in classification: Globular clusters have $R_{1/2} \leq 20 pc$, and dwarf galaxies have $R_{1/2} \geq 100 pc$.

is consistent with many observable phenomena but does not fit at small scales, because it predicts way more dark matter subhalos than the observed one as dwarf galaxies, calling this the "missing satellite" problem. One of the solutions to this problem could be the presence of this hardly observable object, the Ultra faint dwarf in which the re-ionization could have suppressed star formation, so the lack of stars makes this subhalos difficult or impossible to detect. This object could be perfect to demonstrate the existence of True Fossils, galaxies that formed most of their stars before re-ionization.

So the UFD is an object that has either a dynamical mass significantly larger than its baryonic mass or a nonzero spread in stellar metallicities to qualify as a galaxy. This criteria directly indicates the presence of dark matter (for which there is no evidence in globular clusters), whereas the latter indirectly suggests that the object must be embedded in a dark matter halo massive enough that supernova ejecta can be retained for subsequent generations of star formation. By this 21 satellites can be regarded as spectroscopically confirmed UFD galaxies: Segue 2, Hydrus 1, Horologium I, Reticulum II, Eridanus II, Carina II, Ursa Major II, Segue 1, Ursa Major I, Willman 1, Leo V, Leo IV, Coma Berenices (Com Ber), Canes Venatici II (CVn II), Boötes II, Boötes I, Hercules, Pegasus III, Aquarius II, Tucana II, and Pisces II. Satellites that

may be dwarfs but for which either no spectroscopy has been published or the data are inconclusive include the following 21 systems: Tucana IV, Cetus II, Cetus III, Triangulum II, DES J0225+0304, Horologium II, Reticulum III, Pictor I, Columba I, Pictor II, Carina III, Virgo I, Hydra II, Draco II, Sagittarius II, Indus II, Grus II, Grus I, Tucana V, Phoenix II, and Tucana III. The most extended of these objects, such as Tucana IV, Cetus III, Columba I, and Grus II, are perhaps the most likely to be dwarfs given their large radii.

A homogeneous analysis of the structural properties of the early SDSS UFDs was provided by [Martin et al. \(2008\)](#). [Muñoz et al. \(2018\)](#) recently updated this work, presenting uniform processing of deep photometry for all UFDs known as of mid-2015. Confirmed UFDs have half-light radii ranging from 24 pc (Segue 1) to 295 pc (UMa I), with candidate UFDs extending down to 15–20 pc in a few cases. In comparison, the classical dSphs have half-light radii between 170 pc (Leo II) and 2660 pc (Sagittarius). Apart from simply being smaller on average, it has also been suggested that the faintest galaxies have significantly larger ellipticities than larger systems ([Martin et al. \(2008\)](#)). Updating the samples from what was available ten years ago, we calculate a weighted average ellipticity for the UFDs of 0.50 ± 0.01 , whereas the weighted average ellipticity of the classical dSphs is 0.350 ± 0.003 , which is in good agreement with the statistics determined by [Martin et al. \(2008\)](#). However, using a two sided Kolmogorov–Smirnov test, we find that there is a 19% probability that the two samples are drawn from a common distribution. Several analyses of simulated photometric data sets of faint dwarfs have shown that these apparently irregular shapes are the result of Poisson fluctuations in the distribution of stars in the lowest surface brightness regions of these systems rather than evidence for disturbed morphology ([Martin et al. \(2008\)](#), [Muñoz et al. \(2010\)](#)). The recent discovery of the relatively luminous ($M_V = -8.2$), but extremely diffuse, Crater II dwarf ([Torrealba et al. \(2016\)](#)) highlights the possibility that the currently known population of dwarf galaxies may be limited in surface brightness by the sensitivity of existing photometric survey.

Motivated by the results of [Martin et al. \(2008\)](#) for SDSS and [Bechtol et al. \(2015\)](#) and [Drlica-Wagner et al. \(2015\)](#) for DES, we assume that a satellite must contain at least 20 stars brighter than the detection limit of the survey in order to be identified. We create realizations of satellites with stellar masses corresponding to absolute magnitudes of $M_V = -2, -4$, and -6 by randomly selecting the appropriate number of stars from an old, metal-poor mock stellar population. By this, we can observe [Figure 1.6](#) the discovery potential of future imaging surveys.

1.3.1 Stellar kinematics and metallicities

The first important step in clarifying the nature of the UFDs was to determine their stellar velocity dispersions. By measuring the velocities of individual stars in several systems, these early studies constrained their dynamical masses and dark matter content. The initial spectroscopic observations of UFDs were made by [Kleyna et al. \(2005\)](#) for Ursa Major I (UMa I) and [Muñoz et al. \(2006\)](#) for Boötes I (Boo I). Using spectra of five stars from the High-Resolution Echelle Spectrometer (HIRES) on the Keck I telescope, [Kleyna et al.](#) measured velocity dispersion of $\sigma = 9.3_{-1.2}^{+1.7} \text{ km s}^{-1}$. [Muñoz et al. \(2006\)](#)

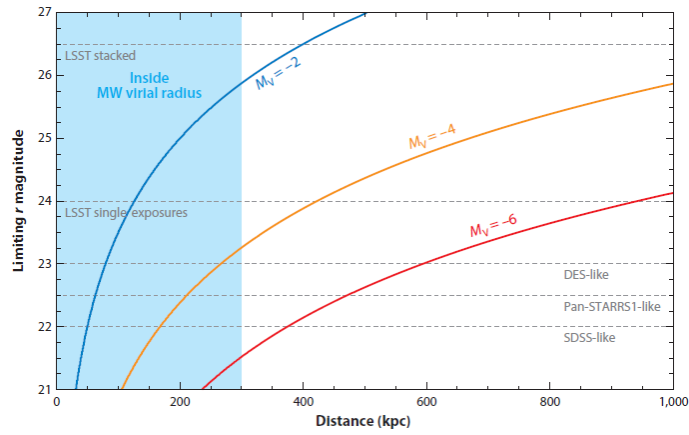


Figure 1.6: Detectability of faint stellar systems as functions of distance, absolute magnitude, and survey depth. The red curve shows the brightness of the 20th brightest star in an $M_V = -6$ object as a function of distance. The orange and blue curves show the brightness of the 20th brightest stars for $M_V = -4$ and $M_V = -2$ systems, respectively. The horizontal dashed lines indicate (from bottom to top) the limiting r magnitude for dwarf galaxy searches in SDSS, Pan-STARRS, DES, and LSST single exposures, as well as stacked LSST images at the end of the survey. The region within the (approximate) virial radius of the Milky Way is shaded blue. Abbreviations: DES, Dark Energy Survey; LSST, Large Synoptic Survey Telescope; Pan-STARRS, Panoramic Survey Telescope & Rapid Response System; SDSS, Sloan Digital Sky Survey.

determined a velocity dispersion of $\sigma = 6.6 \pm 2.3 \text{ km s}^{-1}$ with spectra of seven Boo I stars from the Hydra spectrograph on the Wisconsin, Indiana, Yale, NOAO(WIYN) telescope. These two systems have luminosities of 9,600 and 21,900 L_{\odot} , respectively. If the stellar mass-to-light ratio is $= 2 M_{\odot}/L_{\odot}$, then the expected velocity dispersions from the stellar mass alone would be $\leq 0.1 \text{ km s}^{-1}$. In both cases, such a small velocity dispersion can be ruled out at high significance, demonstrating that under standard assumptions UFDs cannot be purely baryonic systems. Similar conclusions quickly followed for the remaining UFDs based on analyses of spectroscopy by [Martin et al. \(2007\)](#) and [Simon & Geha \(2007\)](#) using the Deep Imaging Multi-Object Spectrograph (DEIMOS) on the Keck II telescope. At the present, velocity dispersion measurements or limits have been obtained for 27 out of 42 confirmed or candidate UFDs.

Once the assumptions of dynamical equilibrium and minimal contamination by binary stars and foreground stars are made, the observed velocity dispersion can be used to constrain the mass of a dwarf galaxy. [Wolf et al. \(2010\)](#) showed that for dispersion-supported stellar systems with unknown velocity anisotropy, the mass that is most tightly constrained by stellar velocity measurements is the mass enclosed within the three-dimensional half-light radius of the system, this approach still requires that the velocity dispersion profile be approximately flat in the measured region (which is generally the case in the dwarf galaxies for which that measurement can be made), but does not assume anything about the shape of the anisotropy profile or the mass distribution. According to [Wolf et al. \(2010\)](#):

$$M_{\frac{1}{2}} = 930 \left(\frac{\sigma}{\text{km s}^{-1}} \right) \left(\frac{R_{\frac{1}{2}}}{\text{pc}} \right) M_{\odot}$$

Where σ is the velocity dispersion and $R_{\frac{1}{2}}$ is the projected two-dimensional half-light radius. Every UFD for which the velocity dispersion has been measured has a mass of at least 105 M_{\odot} within its half-light radius. Among the five systems with only upper limits on the dispersion available, all but Tucana III (Tuc III) are consistent with such masses as well. In comparison, the luminosities are a factor of ~ 100 or smaller.

Correlation between the stellar mass or luminosity of a galaxy and its mean metallicity has been known for decades, [Kirby et al. \(2008\)](#) showed that such a relationship also exists more than five orders of magnitude in luminosity below the regime examined by [Tremonti et al. \(2004\)](#). [Kirby et al. \(2013\)](#) carefully quantified the stellar mass–metallicity relation for Local Group dwarfs, demonstrating that a single relation holds for all types of dwarf galaxies throughout the Local Group:

$$\left[\frac{FE}{H} \right] = (1 - 68 \pm 0.03) (0.29 \pm 0.02) \log \left(\frac{L_V}{10^6 L_{\odot}} \right)$$

with a standard deviation around the fit of only 0.16 dex. The existence of a tight correlation between luminosity and metallicity argues against severe tidal stripping of the stellar components of dwarf galaxies. Tidal stripping reduces the luminosity of a system without significantly changing its metallicity. Stripping, therefore, tends to

increase the scatter in the correlation; indeed, the two dwarfs known to be stripped because of the presence of substantial tidal tails, Sagittarius and Tuc III, lie ~ 0.8 dex and ~ 0.5 dex above the correlation, respectively. The reader may observe that the scatter in the luminosity–metallicity relation appears to increase substantially for UFDs around $M_V \geq -5.5$ and even more so at $M_V \geq -4.0$. This increased dispersion could be interpreted as evidence that the faintest dwarfs have suffered more stripping than the classical dSphs.

1.3.2 Star formation Histories

The first analysis of deep HST imaging of UFDs was carried out by [Brown et al. \(2012\)](#), studying Hercules, Leo IV, and UMa I. They concluded that the three galaxies have similar ages and are each as old or older than the prototypical ancient globular cluster M92. [Brown et al. \(2014\)](#) expanded the sample to six UFDs, adding Boo I, CVn II, and Com Ber to the previous three. [Brown et al. \(2014\)](#) determined that all the galaxies except UMa I had formed more than 75% of their stars by $z \sim 10$, using a star-formation model consisting of two bursts, the best fit for UMa I has approximately half of its stars forming at $z \sim 3$. A large majority of the stars in all six dwarfs had formed by the end of reionization at $z \sim 6$, consistent with the idea that gas heating by reionization ended star formation in such objects. Star-formation histories have also been derived for Hercules, Leo IV, and CVn II by [Weisz et al. \(2014\)](#) from shallower HST data obtained with the Wide Field Planetary Camera 2 (WFPC2). [Weisz et al. \(2014\)](#) found that $>90\%$ of the stars in Hercules and Leo IV are older than 11 Gyr, which is consistent with the [Brown et al. \(2014\)](#) results. In CVn II, however, Weisz et al. concluded that star formation continued until ~ 8 Gyr ago, which conflicts with the findings of Brown et al. The reason for this discrepancy is not clear. Age estimates based on deep ground-based imaging are generally consistent with the HST results, although the constraints are not as tight. Based on the available data, it appears likely that UFDs are uniformly ancient, with all or nearly all of their stars forming in the early Universe. Although most or all UFDs exhibit a blue plume of stars brighter than the main sequence turnoff, this population is best interpreted as blue stragglers rather than young stars.

Their low metallicities make UFDs some of the most extreme environments in which star formation is known to have occurred. They, therefore, present a promising opportunity to investigate how the stellar Initial Mass Function (IMF) depends on the galactic environment. Dwarf galaxies also offer the advantage that their low stellar densities mean that no dynamical evolution has occurred, unlike in globular clusters, so the present-day mass function can be assumed to match the initial one below the main sequence turnoff. [Geha et al. \(2013\)](#) measured the IMF in two UFDs, Hercules and Leo IV, using star counts from the photometry of Brown et al. (2012). Over the mass range of $\sim 0.5\text{--}0.8 M_V$, they found that the best fitting power law had a slope of $\alpha = 1.2$.

1.3.3 Dark Matter

The nature of dark matter is one of the most significant outstanding questions in astrophysics, and the smallest dwarfs may play an outsized role in helping to answer it. In this section, we mention some of the ways in which UFDs can constrain dark matter

properties and dark matter models. UFDs can potentially provide insight into the dark matter for the following several reasons:

- UFDs are the most dark matter–dominated systems are known. Unlike in larger and more luminous dwarfs (e.g., [Brooks & Zolotov \(2014\)](#), [Di Cintio et al. \(2014\)](#)), their baryonic components are likely to have been dynamically negligible at all times. Their inefficient star formation means that feedback should not be powerful enough to alter their internal density structure ([Oñorbe et al. \(2015\)](#)).
- Because of their small sizes, UFDs offer probes of dark matter on smaller scales (20-30 pc for the most compact UFDs) than is possible anywhere else.
- The number of dwarf galaxies orbiting the MilkyWay sets a lower bound on the abundance of low-mass dark matter subhalos, which translates to a limit on the allowed mass of warm dark matter particles.
- Except for the Galactic Center and Sagittarius (which they greatly outnumber), UFDs are the closest dark matter halos to us. The combination of their proximity, their high measured densities ([Simon & Geha \(2007\)](#)), and their low astrophysical backgrounds makes them promising targets for indirect detection experiments.
- The internal dynamics of UFDs are so gentle that heating by very weak effects is potentially measurable. For example, [Brandt \(2016\)](#) used the presence of a star cluster in Eridanus II to place tight constraints on MACHO (massive compact halo object) dark matter, and [Peñarrubia et al. \(2016\)](#) proposed that wide binary stars may be disrupted by the dark matter potential of a UFD, allowing a measurement of the dark matter density profile.

Because of the arguments listed above, UFDs have attracted a great deal of attention from a broad cross-section of astrophysicists. Their potential to facilitate the indirect detection of dark matter has been a particular focus of recent work. The holy grail for dark matter research in dwarf galaxies is the conclusive measurement of the inner density profile of a highly dark matter–dominated system. As mentioned above, UFDs are ideal in the sense that they have the highest known dark matter fractions of any galaxies, and their density structure is unlikely to have been affected by stellar feedback. Their disadvantage is that they contain so few stars that there may not be enough dynamical tracers for robust measurement of the mass distribution. Given the difficulties encountered in analyzing radial velocity data sets containing hundreds to thousands of stars in the classical dSphs, the maximum achievable sample of ~ 100 stars in the most accessible UFDs will not be sufficient to separate a central dark matter cusp from a core. However, the combination of radial velocities and proper motions can provide much more accurate measurements.

1.4 Bootes 1

Many recent studies available on Bootes I: Photometric and stellar population studies have been completed by [Hughes et al. \(2008\)](#). RR Lyrae variability studies by [Siegel](#)

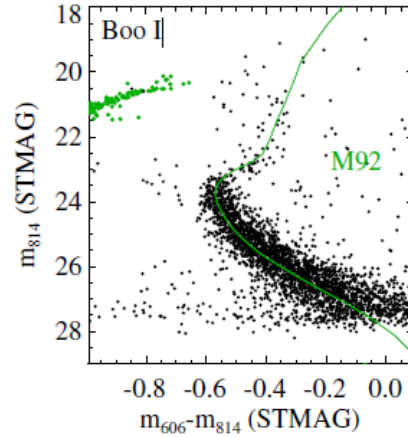


Figure 1.7: CMD Bootes 1 from Brown et al (2014). Green point stars and isochrone of m92. The similarity of the trend shows that both are dominated by ancient metal-poor stars.

(2006); Dall’Ora et al. (2006); Spectroscopic abundance studies by Muñoz et al. (2006); Martin et al. (2007); Norris et al. (2008); Norris et al. (2010b); Norris et al. (2010a).

The first observation and study of Bootes I was done by Belokurov et al. (2006), and data were obtained by SDSS produced in five photometric bands. From this study was possible to reproduce the morphology and so spatial distribution of Bootes I’s stars and even an approximate CMD.

In particular, we can analyze the paper by Brown et al. (2014), for his study used deep optical images in F606W and F814W obtained in 2012. These galaxies were chosen to provide a representative sample of UFD with integrated luminosities bright enough to provide sufficient numbers of stars for the SFH analysis. The goal was to obtain photometry with a high signal-to-noise ratio ($S/N = 100$) for more than 100 stars within 1 mag of the MS turnoff, this allows us to define the age of stellar populations, but for old age, the changes are very small. The scarcity of bright stars prevented the construction of an accurate PSF, so a spatially dependent PSF model was constructed from all of the tiles in a given band, selecting isolated bright stars from each tile. Studying the CMD two aspects can be studied Figure 1.7:

1. the tight stellar locus of each CMDs resembles that if a GC.
2. All the CMD of UFD galaxies seem very similar to each other, implying similar age and metallicities.

In the case of Bootes I, which is relatively nearby, field contamination is high. There are also a few blue stragglers (BS), common stars in ancient populations, that can mimic a much younger sub-population. The combined study of spectroscopy and photometry showed that this UFD is ancient and metal-poor, this can be observed by a proper comparison with M92 one of the most ancient and metal-poor stellar systems

known. Figure [1.7](#) Due to the scarcity of HB stars in the UFD, the HB of M92 can be observed without confusion, from the few HB stars in the CMD there is good agreement between M92 and Bootes 1. However, the earlier evolutionary phases in each UFD are well populated, so the SGB-RGB stellar locus of M92 is shown as a ridge line. The UFD RGB stars are also scattered to the blue of the M92 ridge line. Still, they are not easy to quantify due to the contribution of the asymptotic giant branch star and field contamination, and the lower MS of Bootes 1 scatters to the red of the M92 ridge line, due to the difference in the binary fraction that for the UFD is nearly 50% higher than M92 binary fraction 2%.

Globular clusters are useful empirical population templates for comparison to the UFDs, but the known cluster does not span the full range of age and metallicity required to quantitatively analyze the UFD populations. In particular, the UFD population extend to much lower metallicities, this is the reason why the quantitative analysis employs theoretical models. These models are generated using the Victoria-Regina isochrone and interpolation codes, developed for a wide range of stellar population studies. This isochrone grid spanning $-1 > [\text{Fe}/\text{H}] > -4$, and $8 < \text{age} < 14.5$ Gyr, and $[\alpha/\text{Fe}] = +0.4$ as appropriate for old metal-poor populations, this are appropriated for most of the UFD but in the case in which $[\text{Fe}/\text{H}] > -2$, the UFD may have $[\alpha/\text{Fe}] = 0.1-0.2$ dex lower. Adopting this α -element abundances for the most metal-rich stars, the ages for such stars would be 0.2-0.4 Gyr older, due to the change in oxygen abundance, which affects the rate of the CNO cycle, so the presence of oxygen will impact the MS lifetime and the relation between turnoff luminosity and age. The stars of the diffuse halo $[\text{O}/\text{Fe}]$ appear to increase at decreasing metallicities Figure [1.8](#) So the isochrone that matches a particular CMD will be younger as the oxygen abundance increase with a difference of 1 Gyr per 0.5 dex change in $[\text{O}/\text{Fe}]$. Considering the M92 isochrones match at 13.2 Gyr with an uncertain at the level of 1 Gyr due to composition, reddening and distance. To fit the observed UFC CMDs, we must convert the isochrone grid into a set of synthetic CMD with the same properties as the observed UFD CMD, this is determined via extensive artificial star tests. Each synthetic CMD represents a stellar population at a single age and metallicity, a combination of this can be used to fit the observed UFD CMD. The synthetic CMD set for each galaxy is calculated using the measured distance, reddening values and also fixed field contamination component.

The comparison of the observed CMD to the synthetic demonstrates that the observed one can be reproduced with a very simple model, that includes two episodes of star formation. The fit has three parameters: the ages of the two components and the fraction of star formation in each. Each episode is a single-age population but can have a range of metallicities. In Figure [1.9](#) is show a comparison of the observed UFD CMD to the best-fit synthetic CMD, represented as a two-dimensional distribution of probability density.

To this fits two additional parameters can be added, varying the duration of star formation in each of the two bursts, not improving the fit quality. The resulting five-parameter fits minimize the duration of star formation in each burst and do not improve the Poisson maximum likelihood statistic (PMLS) underscoring the preference for a narrow age range in each burst. The two-burst model is a better match to each CMD than a model with a single burst and has the advantage of quantifying the possible contribution of a minority population, in the case of BOOTES 1 the two components

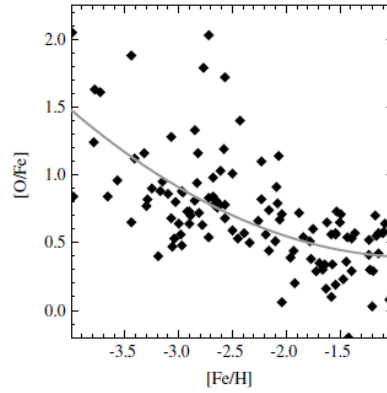


Figure 1.8: Oxygen abundance as a function of metallicity, as observed for metal-poor stars in the halo and satellites of the Milky Way abundance scale.

are essentially the same age. If the star formation history is adapted to a single age, this will happen within 0.2 Gyr of the mean age in a two-burst model. Studying the best-fit models a significant fraction of the population is approximately as old as the universe.

The spectroscopy demonstrates that these galaxies are comprised of extremely metal-poor stars, this factor is consistent with the pre-enrichment from a single supernova. Using these metallicities as a constraint in fits CMDs, UFD galaxies are well matched by a population of ancient stars. The majority (75%) of the stars formed prior to $z = 10$ (13.3 Gyr ago) when the epoch of re-ionization began. The population of this galaxy were influenced by even that sopped the star formation.

Another important study was done by [Koposov et al. \(2011\)](#), studying the velocity dispersion and the velocity errors of the system. The main problems that had to face observing a UFD were:

- The very small number of stars 10^{2-4} , so for some objects the number of available targets for spectroscopic observation is limited to a few tens of predominantly faint stars, for which radial velocity errors may be of the order of or larger than the velocity dispersion of the system.
- Measuring the small velocity dispersions using a small number of stars, because is still unclear how much they can be affected by the binary stars which must be in the sample.

With this study they had two ambitions:

- Improve the knowledge of the Bootes I dSph galaxy.
- Improve the knowledge of how reliably and accurately we can measure radial velocities of dSph member stars.

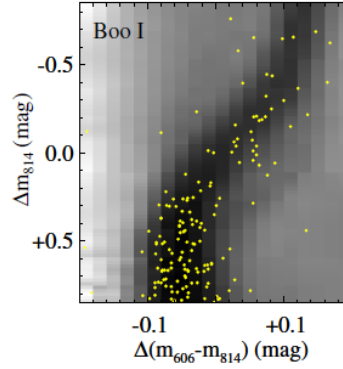


Figure 1.9: Observed CMD (yellow points) compared to the probability cloud for each associated best-fit model. The plots here are centred on $M_{606}-M_{814} = -0.55$ mag and $M_{814} = 3.95$.

Kinematic studies of ultra-faint dSphs are especially challenging due to the fact that the measured velocity dispersion, the typical errors of individual velocities, and the expected contribution of binary stars are all similar, at a few km/s. The previously studied SDSS dSphs have reported velocity dispersion as small as 3 km s^{-1} (Simon & Geha (2007)). McConnachie & Côté (2010) demonstrate that for such cold dispersions, it is difficult to disentangle contributions from random (i.e., reflective of the underlying gravitational potential) and binary-orbital motions. In such a case the velocity dispersion could be substantially lowered than the predicted one. In this situation it is critical to account accurately for velocity errors—when propagated through calculations, optimistic/pessimistic errors result in over-/underestimates of the true velocity dispersions. For this kind of study of specific relevance, two kinematic studies are available.

Muñoz et al. (2006) obtained spectra of red giant branch (RGB) candidates over part of Bootes I, selected from SDSS DR4. They used the WIYN telescope and the Hydra multifiber spectrograph. Their data (for a 7 member-star sub-sample) yielded a systematic velocity of $95.6 \pm 3.4 \text{ km/s}$ and a central velocity dispersion of $6.6 \pm 2.3 \text{ km/s}$. They derived $\sigma_0 = 9.0 \pm 2.2 \text{ km/s}$ from 12 member-star sample. A value which was adopted in a later analysis by Wolf et al. (2010).

Martin et al. (2007) observed candidate Bootes I red giants from SDSS (DR4) with Keck/DEIMOS, finding a mean velocity of $99.9 \pm 2.4 \text{ km/s}$, with central velocity dispersion $\sigma = 6.5^{+2.1}_{-1.3} \text{ km/s}$ for their final sample of 24 member stars.

From their kinematics, Muñoz et al. (2006) deduced a mass of $1.1^{+1.3}_{-0.5} \times 10^7 M_{\odot}$. Wolf et al. (2010) adopt the high-velocity dispersion of $9.0 \pm 2.2 \text{ km/s}$, by accepting the superset of the data of Muñoz et al (2006). From this, they deduce a correspondingly higher mass.

In summary, Bootes I is some 65 kpc ($m-M = 19.07$) distant, has absolute luminosity

$M_{V,\odot} = -5.9$, is devoid of HI, has somewhat elliptical (ellipticity =0.2) morphology, has a half-light radius of 240 pc, has an apparently exclusively old metal-poor stellar population, with a significant blue straggler sub-population, has a mean [Fe/H] metallicity of -2.55, has an intrinsic abundance dispersion with formal $\sigma = 0.45$, with a range in [Fe/H] of at least 1.7dex, and has at least one member star which has [Fe/H]= -3.7. It is at an intermediate distance from the Galactic centre (70 kpc Galacto-centric), far enough that tidal effects need not be dominant, yet close enough that observations far enough down the giant branch to obtain useful statistical samples are feasible, in spite of its (interestingly) low intrinsic luminosity. It has extremely low surface density, so it is a clear test case for galaxy formation models, none of which naturally creates very large, very low surface brightness galaxies. The abundance results suggest Bootes I is a survivor of a true primordial system, quite likely forming prior to reionization, enhancing its interest. Its velocity dispersion is reported as being at least 6 km/s, a value which is feasible to measure with high accuracy. It seems to have an extremely high apparent mass-to-light ratio, again enhancing its intrinsic interest. It is visible from the VLT.

To retrieve information about the kinematic of Bootes I they selected target stars with a sufficiently wide range of apparent magnitude that a single observation of the brightest stars would provide a similar signal-noise ratio to the final signal-noise ratio of the fainter stars, integrated over 16 identical single exposures. By comparing the actual repeatability of velocities for the brighter stars, we could verify if the deduced accuracy calculated for the faintest stars was reliable. Additionally, by summing the brighter star exposures, they could readily test for any systematic floor in delivered accuracy at some high signal-noise value. They used the FLAMES spectrograph at the 8.2-m Kueyen (VLT/UT2) telescope at Cerro Paranal, Chile, to acquire spectra of individual stellar targets in Bootes I. Observations took place in service mode during 2009. In order to maximize the probability of observing Bootes I members, they selected stellar targets based on the colors and magnitudes of the stars. The left-hand panel of Figure 1.10 displays the color-magnitude diagram (CMD) of all stars (including foreground) within 12 arcmins of the centre of Bootes I. Recall that the half-light radius of Bootes I is greater than 12 arcmin - they are sampling only the very inner regions in this (first) study. As the RGB of Bootes I together with a few blue horizontal branch stars (BHB) are clearly visible on the left panel of Figure 1.10. The middle panel of Figure 1.10 plots the CMD for our FLAMES targets, which include stars up to two magnitudes fainter than the horizontal branch. The second compromise involved the trade-off between target numbers and adequate data to test our delivered velocity accuracy. In order to obtain useful spectra for the faintest targets, and to implement our test of achievable precision, we observe only a single field with a single target configuration centred on Bootes I.

Two observational kinematic studies of Bootes I (Muñoz et al. (2006); Martin et al. (2007)), and two other analyses (Wolf et al. (2010); Norris et al. (2010b); Norris et al. (2010a)), have been published, providing information which we may compare with our results.

Muñoz et al. (2006) used the WIYN telescope and the Hydra multifiber spectrograph to measure radial velocities for 58 candidate member stars, all brighter than $g=19$. Considering the strength of the Mgb absorption features, they classify fully 30 of these

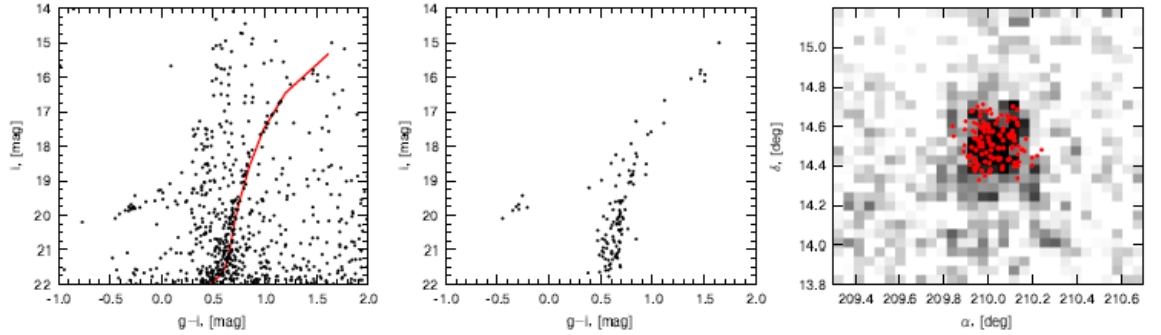


Figure 1.10: Left panel: Color-magnitude diagram of all objects classified as stars with good photometry in a 12 arcmin square area centred on Bootes I, from SDSS. The line shows the fiducial RGB sequence for the metal-poor globular cluster M92 (from Clem et al. (2008)), placed at the distance of Bootes I dSph. Middle panel: The colour-magnitude diagram of candidate stars targeted for VLT spectroscopy. Right panel: The density of SDSS stars around the center of Bootes I is shown in grayscale, the targeted stars are shown by red points. For comparison, the half-light radius of Bootes I is 12.5 arcmin.

as giants. Further considering the position, velocity and line strength, they identify seven stars located within 10 arcmin of the centre of Bootes I to define the mean velocity and velocity dispersion of Bootes I, finding a mean velocity 95.6 ± 3.4 km/s, and central velocity dispersion 6.6 ± 2.3 km/s. With these values, they further identify a total of 12 stars as “potential 3σ members”, 11 being within a radius of 15 arcmin of the centre of Bootes I, the 12th at 27 arcmin distance (the half-light radius is 12.5 arcmin). These 12 candidate members provide a higher mean velocity, 98.4 ± 2.9 km/s, and a higher dispersion of $\sigma_0 = 9.0 \pm 2.2$ km/s; this higher dispersion, as the authors note “corroborating the apparent increase of the velocity dispersion with radius”. The full set of stars provides a velocity dispersion of $\sigma_0 = 14.6 \pm 3.0$ km/s, suggesting “a possibly dramatic increase of the Boo velocity dispersion with radius”. The 12-star sample, with its Bootes I velocity dispersion of $\sigma_0 = 9.0 \pm 2.2$ km/s, is that adopted by Wolf et al. (2010) in their dynamical analysis. The comparison between Koposov and Munoz can be observed in Figure 1.11, in this case, the results are inconsistent with the velocity dispersion reported by Munoz.

Martin et al. (2007) observed 96 candidate Bootes I red giants from SDSS (DR4) with Keck/DEIMOS. They identified a sample of 24 member stars, each with a radial velocity determined with an accuracy smaller than 6 km/s. From this sample, they find a mean velocity of 99.9 ± 2.4 km/s, with central velocity dispersion $\sigma_0 = 6.5^{+2.1}_{-1.3}$ km/s for their final sample of 24 stars with small velocity uncertainties. Koposov et al. observed 27 common stars, plotted in the rightmost two panels of Figure 1.11. In which can be observed that the zero points of the radial velocity measurements are consistent. The mean velocities are $V_{keck} = 99.6 \pm 1.6$ km/s and $V_{VLT} = 101.8 \pm 0.7$ km/s. The right-hand panel of Figure 1.11 compares the derived velocity errors with those reported by

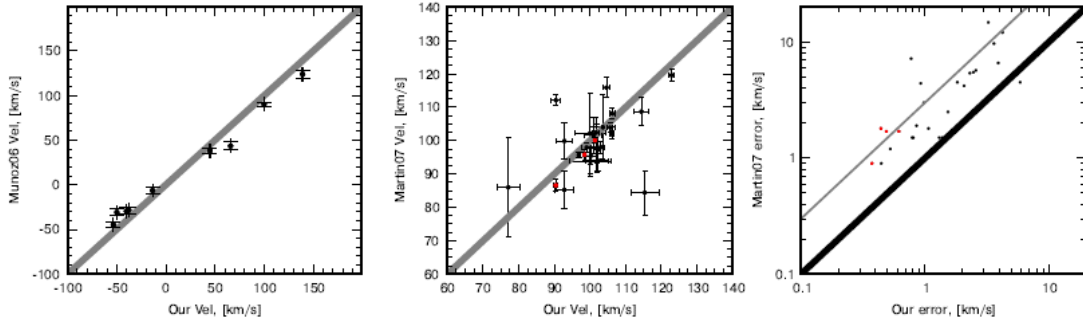


Figure 1.11: Left panel: Comparison of Kuposov et al. velocity measurements for 9 stars in common with the velocity measurements of Munoz et al. (2006). The line shows the expected one-to-one relation. The data sets are apparently not consistent with the published errors and suggest a velocity-dependent scale error. Middle panel: Comparison of Kuposov et al. velocity measurements for 27 stars in common with the velocity measurements of Martin et al. (2007). The line shows the expected one-to-one relation. The red points identify stars which may have variability in radial velocities. Right panel: Comparison of Kuposov et al. radial velocity errors with those of Martin et al. (2007). The thick black line shows the one-to-one relation, while the grey line shows the $y = 3x$ relation.

Martin et al. (2007). And the derived single-velocity errors are a factor of about two smaller than those of Martin et al. (2007), at high signal-noise ratios in both studies. The velocity difference, in units normalised by the quadrature sum has a sigma of 2.7, robust evidence that the combined errors are underestimated.

By making 16 individual repeat observations over six weeks, with a wide dynamic range in each observational data set, they have reached several goals: most importantly, they have been able to properly assess the errors of their radial velocity measurements; they delivered radial velocity precision, for faint extremely weak-lined stars, is better than 1 km/s for the combined exposures. Second, they have been able to identify and reject stars that show significant radial velocity variability. Comparing the derived velocity dispersion, and individual velocities, with literature studies (Muñoz et al. (2006); Martin et al. (2007)), shows that previous studies have substantially overestimated the velocity dispersion of Bootes I. It is possible that earlier studies underestimate their velocity errors, and hence overestimate the velocity distribution which is deconvolved from those errors.

The data also provide direct limits on kinematic gradients in Bootes I. Our formal limits on rotation are: minor axis, -4 ± 9 km/s/deg; major axis 0 ± 8 km/s/deg. Similarly, any radial change can be limited in dispersion. However, fitting a single Gaussian dispersion to the inner half-radius and outer half-radius provides a formal, statistically insignificant, radial decrease in the dispersion of 2.1 ± 1.3 km/s.

We consider now the possibility that the higher velocity dispersion component in Bootes I kinematics is an artefact of unresolved binaries with variable radial velocities. A hypothetical substantial population of binaries with velocity amplitudes of order

10 km/s, and periods much longer than a month, might produce spurious wings in the radial velocity distribution which we would identify as a hotter component, but Figure 1.11 limits the plausibility of this speculation. For Bootes I we seem to have two dispersions, with no robust way to associate a scale length with either. If we just assume that the dominant low dispersion component is associated with the measured half-light radius, then we can (very approximately) deduce an associated mass within that radius of 240pc. Adopting the low dispersion computed by Koposov et al of $\sigma_v = 2.4$ km/s provides a mass lower than that of Wolf et al. (2010) by a factor of 14, and a corresponding $M/L = 120$.

The data suggests that the Bootes I dwarf spheroidal has both cold and hot stellar components. If we divide the 16 stars into equal inner and outer groups of eight stars based on radius from the centre of Bootes I, the inner and outer groups have mean abundances $[Fe/H] = -2.30 \pm 0.12$, and $[Fe/H] = -2.78 \pm 0.17$ respectively. These differ at the 2.4σ level.

A plausibility argument of relevance to this speculation is that the lowest luminosity dSphs are systematically less round than are more luminous galaxies - although Bootes I itself has ellipticity 0.2, so is relatively round. It is often assumed that dSph shapes correspond to the shapes of the dominant dark matter distributions. One option is that there is a two-component structure in Bootes I, with future observations at large Bootes-centric distances required to identify the characteristics of the higher-velocity dispersion population, which is a minority in the inner regions, and which must have a hugely extended radial scale length. Alternatively, Bootes I has a velocity distribution function which reflects its formation, which is a combination of a majority population with very radially-biased orbits, and a minority population with very tangentially biased orbits. Both are represented by a single, measured, radial scale length. The more radially-biased population contains the most metal-poor star

1.5 Outline and purpose of the Thesis

The aim of the thesis is to give constraints of the proper motion of Bootes I. To do so, a sector of UFD is studied in two different epochs. The outline of the thesis is the following:

Chapter 1 provides a description of the Dwarf galaxies, and how the stellar population change over time. Finally, an overview of the Ultra faint dwarf galaxy and specifically on Bootes I has been made. **Chapter 2** contains a detailed description of the instrumentation used, the sample considered and the photometric and astrometric data reduction performed on Bootes I, while in **Chapter 3** I illustrate the data analysis and the main results of the thesis. Finally, **Chapter 4** provides a discussion about the final results and a comparison with literature results.

Chapter 2

Data and Data reduction

2.1 Instrumentation

2.1.1 Hubble Space Telescope

HST is the only telescope that nowadays can provide the high-precision photometry needed to detect and properly characterize MPs. It orbits around the Earth, avoiding distortions introduced by the atmosphere and therefore obtaining images with higher resolution than that of the majority of ground-based telescopes. Such performance is fundamental to measuring accurate positions and magnitudes of very faint galaxies. Another advantage is that HST can detect photons with wavelengths that are inaccessible to ground-based telescopes due to the opacity of the atmosphere, providing information in bands that are fundamental to detect and characterize MPs, including those inferred from the UV filters. HST has a primary mirror of 2.4 m and covers a wide range of wavelengths, from 100 nm to 1700 nm. In order to detect light in different spectral bands, the telescope has onboard different cameras, each with a certain Field of View (FoV), wavelength range and plate scale (ps). The images used in this work have been obtained with the two following cameras:

- **Advanced Camera for Surveys (ACS)** It has three channels:
 - High-Resolution Channel (HRC), with $\text{FoV} = 29.1 \times 26.1 \text{ arcsec}^2$, covering a wavelength range of 200-1050 nm and with $\text{ps} = 0.027 \text{ arcsec pixel}^{-1}$.
 - Solar Blind Channel (SBC), with $\text{FoV} = 34.59 \times 30.8 \text{ arcsec}^2$, covering a wavelength range of 115 - 180 nm and with $\text{ps} = 0.032 \text{ arcsec pixel}^{-1}$.
 - Wide Field Channel (WFC), with $\text{FoV} = 202 \times 202 \text{ arcsec}^2$, covering a wavelength range of 350 - 1050 nm and with $\text{ps} = 0.05 \text{ arcsec pixel}^{-1}$.
- **Wide Field Camera 3 (WFC3)**. It has two channels:
 - UVIS, for ultraviolet and visible light, with $\text{FoV} = 160 \times 160 \text{ arcsec}^2$, covering a wavelength range of 200-1000 nm and with $\text{ps} = 0.04 \text{ arcsec pixel}^{-1}$.

Table 2.1: Summary of the information about all the images used in the photometric data reduction of Bootes I

DATE	N x EXPTIME	FILTER	INSTRUMENT
12 June 2012	2x430s+2x670s	F814W	UVIS/WFC3
12 June 2012	2x500s+2x670s	F606W	UVIS/WFC3
30 June 2019	4x1258s	F814W	UVIS/WFC3
30 June 2019	4x1224s	F606W	UVIS/WFC3
03 July 2019	2x1258s	F814W	UVIS/WFC3
03 July 2019	2x1224s	F606W	UVIS/WFC3
04 July 2019	2x1258s	F814W	UVIS/WFC3
04 July 2019	2x1224s	F606W	UVIS/WFC3

- NIR, for near-infrared light, with FoV = $123 \times 137 \text{ arcsec}^2$, covering a wavelength range of 850-1700 nm and with $\text{ps} = 0.13 \text{ arcsec pixel}^{-1}$.

2.1.2 GAIA

The Gaia satellite can provide a high-precision astrometric measure and will provide unprecedented positional and radial velocity measurements. It orbits around the L2 point Sun-Earth, in this position Sun Earth, and Moon are outside the observation field. This satellite will be fundamental for the study of proper motions because it can determine the exact position of astrophysical object at different times. Hence it will measure proper motions with an accuracy between 20-200 micro arcsec. It is able to compute the distances of every star, with higher accuracy for closer and brighter ones, and finally studying at different wavelengths in different periods can obtain the radial velocities. The final purpose is to create a 3-Dimensional map of our Galaxy. In the present work/thesis, I will make use of the latest data release, i.e eDR3 to investigate the proper motions of stars in the UFD Bootes I

2.2 Dataset

To investigate the UFD galaxy Bootes I, I made use of HST images, observed through the F606W and F814W filters, in two different epochs, namely 2012 and 2019, and the data by [Brown et al. \(2014\)](#). The main properties of the observations are summarized in Table [2.1](#). The scarcity of bright stars has prevented the construction of an accurate Point Spread Function (PSF), so a spatially dependent PSF model was constructed from all of the tiles in a given band, selecting isolated bright stars from each tile.

2.2.1 Effective Point Spread Function

As discussed in detail in [Anderson & King \(2000\)](#), in a typical HST image, stars appear as relatively isolated point-like sources, so we can describe them by means of three parameters: centre coordinates (x,y) and total flux (f). To derive accurate stellar positions we require a precise PSF model. Inaccuracies can lead to systematic errors

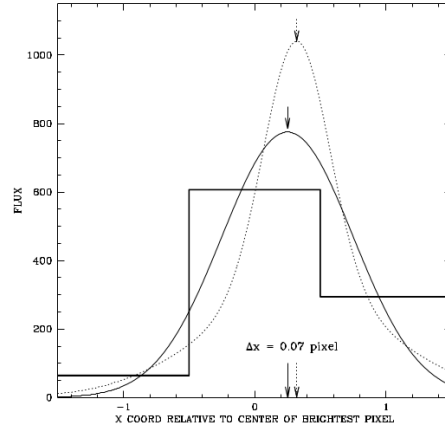


Figure 2.1: The histogram shows the flux value in three adjacent pixels. The two smooth curves represent two different PSF models, which gives different peak (and therefore center) positions (Anderson & King 2000).

in the measurements of stellar positions, as can be seen in Figure 2.1. Such errors are commonly referred to as pixel-phase errors and depend on the location of the star within the pixel. To solve this issue, it is important the following consideration, two dimensional PSF describes how the light of point-like sources is distributed after being processed by a telescope so that each star image is a replica of the PSF with certain values of position and flux. The PSF produced by a telescope at its focal plane is called instrumental PSF (iPSF). It's impossible to observe it directly, but what is observed is an array of pixels, each one with a value of registered counts. The value of counts in a pixel at some offset Δx Δy , from the centre of the iPSF, depends on the results of a convolution between the iPSF and the sensitivity profile of a pixel. The effective PSF (ePSF), as defined in Anderson & King (2000), is this convolution. The ePSF has three major advantages with respect to iPSF:

- **Simplicity.** The fitting of the PSF to a stellar image requires no integration since it consists only in finding the values of x_* , y_* and f_* that minimize the sum of the squares of the residuals
- Easier to solve for an ePSF than for an iPSF. So knowing x_* , y_* and f_* can be derived an ePSF for each pixel.
- **Better accuracy.**

2.2.2 Deriving the effective PSF Model for Bootes 1

To obtain the best possible PSF, and so to obtain the most accurate photometry and astrometry, the techniques presented in Section 2.2.1 are applied. In theory, to derive

an appropriate PSF model we would need stellar position and fluxes, but no position and fluxes can be measured without a PSF model. To break this degeneracy we adopted an iterative procedure.

1. All pixel values in the image are converted to an estimated first-guess position and magnitudes. This is used to derive an improved PSF model that will be used to measure stars in the next iteration.
2. The ePSF is now used to better estimate the position and magnitude of each star
3. The values found are transferred in a common reference frame, combining them and analyzing the residual

These steps are repeated, improving the model until it reaches convergence. The first iteration allows building a model based on the actual image, using the raw position and magnitudes obtained from fitting the PSF library, taking into consideration only the isolated, bright but not-saturated star and not contaminated by cosmic rays stars for each exposure. This is done using the routines `img2psf` (Anderson & King (2000)). These routines find all stars in a certain image that meet some criteria, defined by the following arguments

- **HMIN.** Used to select isolated stars, defines the minimum separation (in pixels) between two sources in order to be considered. A typical value here used is 11.
- **FMIN.** Used to select the minimum value of flux (expressed in counts) that a source can have to be considered. A typical value here used is between 2000-3000
- **PMAX.** Used to select the maximum value of flux (expressed in counts) that a source can have to be considered. Since saturated stars have to be excluded, a typical value here is 54999, immediately below the saturation limit.
- **QMAX.** Used to define the maximum value of the Q parameter, an indicator of the quality of the fit. If it is too high, the sourced fitted is probably not a star. A typical value here used is 0.3.
- **NSIDES.** Used to define how many regions the image has to be divided. Using a lot of different regions helps to take into account variations of the PSF across the chip. The value is kept at 1 for all the images analysed.
- **PSFFILE.** Used to define the initial PSF model.
- **IMG.fits.** Used to define the image on which the procedure is performed.

As represented in Figure 2.2, the program compute a grid of 9x10 PSFs, this is necessary due to the position-dependent charge diffusion and optical aberrations and so the PSF could change its shape with location on the detector.

Once I calculate the PSF models, I used the FORTRAN routine `img2xym` (Anderson & King (2000)) to obtain the positions and instrumental magnitudes of all the stars. To do this, I fit the just-derived PSF models to each image. This time, I did not restrict

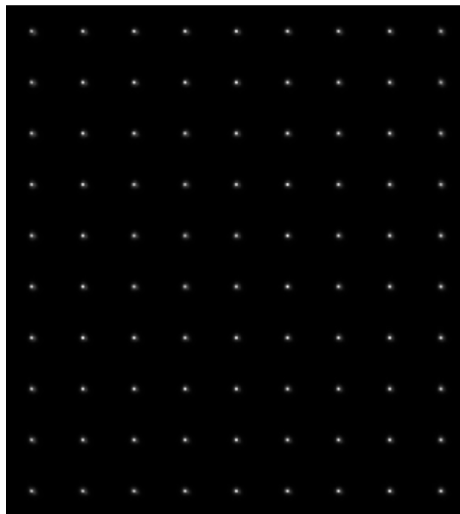


Figure 2.2: An example of ePSF for one of the WFC/ACS images collected through the F606W filter.

the analysis to all stars but measured most of the stars in the image. Specifically, I used an isolation index $\mathbf{HMIN} = 3$ pixel, a minimum flux of $\mathbf{FMIN} = 50$ DN, and included saturated stars ($\mathbf{PMAX} = 999999$). The main final output is a file with .xym extension giving coordinates (x,y), the instrumental magnitude, and the Q parameter, fundamental to discriminate between real stars and other sources in the following,

2.3 Catalog building

To build the astro-photometric catalogs of Bootes I, I adopted the following procedure: every image is reduced singularly and then exposures in each filter are put together. This method is particularly suitable to improve the precision of measurements for bright stars.

2.4 Star Analysis

The files obtained in Section [2.2.2](#) contain all sources that fulfilled all the requirements inserted in the routines, but not all of them are stellar objects. Indeed, in addition to stars, the program measures a variety of non-stellar objects such as cosmic rays, hot pixels, noise spikes, or other artefacts. We used the Q parameter as a diagnostic of the quality of the fit to identify a sample of well-measured stars.

As an example [Figure 2.3](#) we plot the parameter Q derived from F606W photometry as a function of the F606W instrumental magnitude. The red line is drawn by hand with the criteria of separating the bulk of well-measured point-like sources (blue points) from sources that are poorly fitted by the PSF model (black dots).

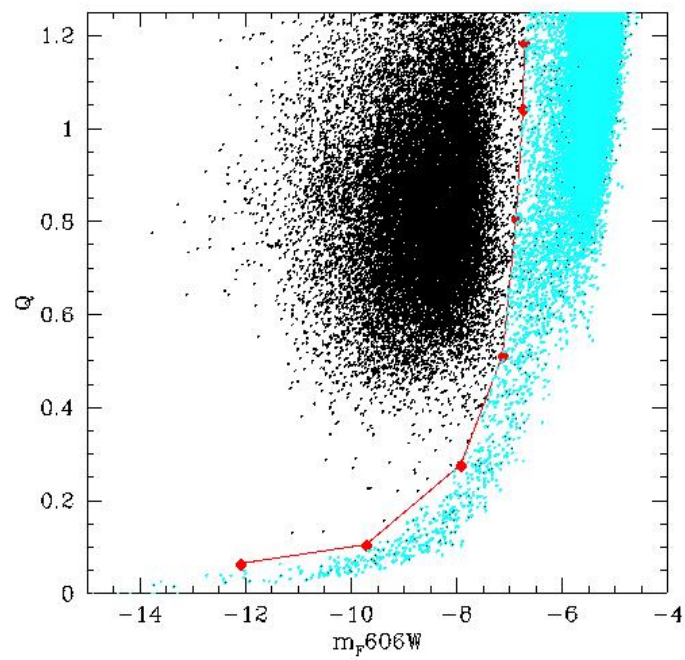


Figure 2.3: In red the fiducial line, blue stars are the ones that are considered real stars, black dots are noise, hot pixels, cosmic rays and PSF artefacts.

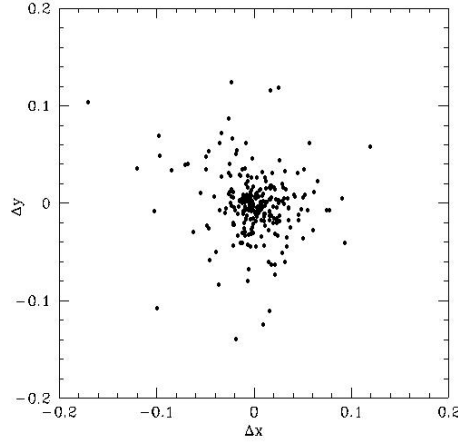


Figure 2.4: Example of transformation residuals between one of the exposure in the F814W filter and the master frame.

The final output of this program is a catalog for every image containing positions and magnitude for all the identified stars.

The following step is to obtain a single catalog for each filter. To do that, an image is selected as the reference frame (master frame), because the different images are not perfectly superimposed, so to bring them into the master reference frame, it is used the routine **xym2mat**, **xym2bar** and **xym1mat** developed by Jay Anderson. Specifically, **xym2mat** finds the same stars in different catalogues through two different iterations:

1. Bright and saturated stars are identified. The program uses a method called *Cross Identification* consisting of looking for similar triangles of stars between the master frame and the analyzed exposure, so it can identify the common objects in different catalogues. Whose coordinates, both in the master and in the image reference frame, are used to calculate, the six coefficients of the transformation that allows bringing all the images in the same reference frame.

$$\begin{cases} x_1 = A Cx_2 E y_2 \\ y_1 = B Dx_2 F y_2 \end{cases}$$

where A, B, C, D, E, and F are the coefficients of the transformation, while (x_1, y_1) and (x_2, y_2) are the coordinate of a star in the two reference frames. So as a final result position and magnitudes of each image can be expressed in terms of the master reference frame.

2. The output is used as a starting point for the second iteration in which the same operation is repeated excluding saturated stars since they are not well measured.

The final output of the procedure is a series of files with the position and magnitude of the common stars and their residuals with respect to the master. Figure [2.7](#)

The **xym2mat** routine requires one argument, that is the distance (in pixels) from a star within which the program searches for common stars. In the first iteration, the distance is kept quite large, while in the second one is smaller. After that, is possible to obtain a catalogue for each filter, using the routine **xym2bar**, developed by Jan Anderson, to compute average positions and instrumental magnitudes of common stars with $\text{mag} < -5.5$, that because this part of photometric reduction works better for bright stars. The program requires one argument, which is the minimum number of different images in which the same star has to be individuated to be considered. It comes from a compromise between having catalogues with a large number of stars or with a few better-measured stars.

Finally, to link catalogues together, to obtain catalogues with star's magnitude in different filters, the routine **xym1mat**, developed by Jay Anderson, has been used. Once chosen a reference catalog (I selected F606W as the master), the software will find common stars between them. The final output is a catalog for each filter linked to the F814W one. Every catalog has its own reference frame, in this case, is the frame 2012 of F606W filter.

Starting from this new master frame, the **xym2mat** and **xym2bar** routines are repeated, obtaining a new F814W catalog for 2012, and both F606W and F814W for 2019. The other filters, linked to F606W (2012), will be tied up using **xym1mat** routine. Using these new catalogues I could represent the first Bootes I CMD surrounded by background and faint stars. Figure [2.5](#).

2.5 Study of the proper motion

2.5.1 Proper motion techniques

Depending on the astrophysical objects selected as reference sources, different procedures can be used to compute the absolute proper motions of a cluster or a galaxy. For instance, if background quasars or galaxies are chosen as reference (see e.g. [Bedin et al., 2003](#); [Milone et al., 2006](#)), then stellar positions are measured for each filter and epoch independently, by using the effective-point-spread function (ePSF) algorithms. To avoid systematic errors, proper motions are calculated using two epochs in the same filter. The ePSF-fitting procedure is used again to find an ideal reference point for the measurement of the absolute proper motions of stars. So after the absolute proper motion is obtained, the mean radial velocity of the cluster can be inferred from its spectra, if available.

In this thesis, I used an alternative approach which is based on the comparison of HST relative and Gaia absolute proper motions. Specifically, after the localization of the field stars, by means of the proper motion analysis, I use GAIA data, e.g. proper motions, to move in an absolute reference frame.

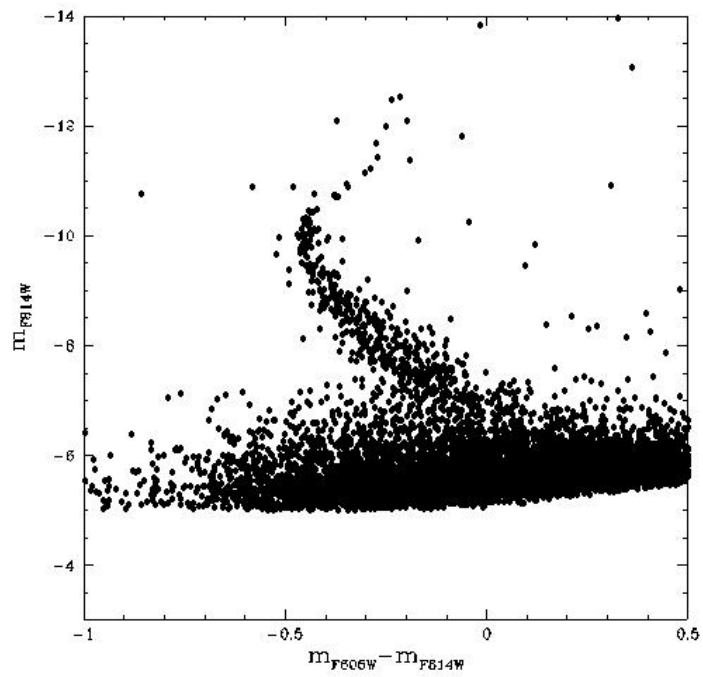


Figure 2.5: CMD made using both filters of 2012. We have a prime example of the CMD surrounded by background and faint stars.

2.5.2 Proper motion Analysis

To compute proper motions I take advantage of having more than one epoch observation with appropriate signal-to-noise ratio and temporal baselines to disentangle the internal kinematics of Bootes I stars and separate cluster members from field stars, by using HST data alone. Relative HST motions are then transformed into absolute motion thanks to Gaia EDR3 proper motions.

To derive relative proper motions we applied to our dataset the procedure described by [Piotto et al. \(2012\)](#). In a nutshell, we first identified the distinct groups of images collected in the same epoch, filter, and camera. We reduced each group of images, separately obtaining the corresponding astrometric and photometric catalogs. The reference frame defined by the first-epoch images collected through the reddest filter is adopted as a master frame. The coordinates of stars in each catalog are transformed into the master frame by means of six-parameter linear transformations, as described in [Section 2.4](#).

Then, I improve the derived catalog by using the Fortran routine **lnk2res**. In this way only bright and unsaturated stars will be used for the transformation. We derived the proper motions relative to a sample of Bootes I members that have been selected in an iterative way. As a consequence, the average relative motion is set to zero. We first identified the probable UFD members as stars that, based on all available CMDs, lie on the main evolutionary sequences and used them to derive initial proper motion estimates. Then, we iteratively excluded those stars that do not share the same motion as the bulk of Bootes I members. So the input used are:

- the catalog previously created by **xym1mat** that correlates positions to the magnitude of the master filter with another one.
- Number of iterations, more iterations will set the position of the stars with better accuracy.
- The radii in which paired stars are searched.
- A file that indicates the well-measured UFD members

The output given is a file in which are marked the shift of the stars, the number of iterations, and the position and magnitude of the stars, these last are information that we can find in the output file of **xym1mat**.

At the end of the process will get three different files, one for each linked catalogue I had:

- Stellar displacements obtained from the match between the epoch 2012 in the filter F606W and the epoch 2012 F814W.
- Stellar displacements obtained from the match between the epoch 2012 in the filter F606W and the epoch 2019 F606W.
- Stellar displacements obtained from the match between the epoch 2012 in the filter F606W and the epoch 2019 F814W.

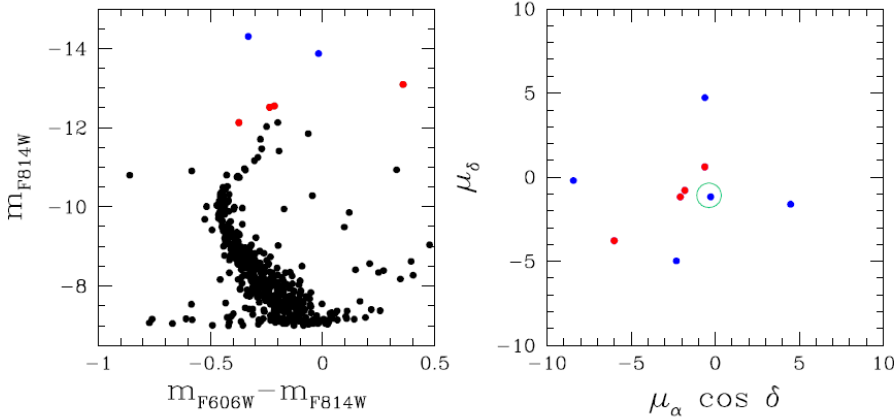


Figure 2.6: The left plot represents the CMD of BootesI, and the right plot represents the absolute proper motions. Black dots are stars that belong only to HST data, red dots are stars in common for HST and Gaia, not saturated for HST. Blue dots represent common stars but are saturated for HST and the green circle is the range of stars that are compatible with the proper motion of Bootes I. We can observe that there are more bright stars in the plot of the proper motions with respect to the plot of the CMD, that because almost all stars have magnitude < -14 and are extremely saturated for HST.

Now to estimate the absolute proper motions, we have to combine information from HST and GAIA EDR3 proper motions. We selected by eye stars that are probable UFD's members. Then, we used the Gaia EDR3 catalogue to select stars with a specific range of magnitudes. The average proper motion has been calculated as the $3\text{-}\sigma$ clipped average of the proper motions of the UFD members for which are available both HST photometry and GAIA EDR3 high-quality proper motions.

So to transform relative proper motions into absolute ones we derived the difference between the relative proper motions derived from HST images and the absolute proper motion from Gaia EDR3 for an appropriate sample of stars. Specifically, this selected sample includes stars with high-quality relative proper motions.

The main steps of the procedure used to derive the absolute proper motion are illustrated in Figure 2.6, in the CMD are selected by eye the stars based on their colours and magnitudes, are located on the main evolutionary sequences. In our case, we have a high number of extremely bright stars in common. In Figure 2.6 the left plot represents the CMD of Bootes I, and the right plot represents the absolute proper motions diagram. Black dots are stars that belong only to HST data, red dots are stars in common for HST and Gaia, not saturated for HST. Blue dots represent common stars but are saturated for HST and the green circle is the range of stars that are compatible with the proper motion of Bootes I. We can observe that there are more bright stars in the plot of the proper motions with respect to the plot of the CMD because almost all stars have magnitude < -14 and are saturated for HST. Table 4.1

We refer to papers by [Cordoni et al. \(2020\)](#) and [Cordoni et al. \(2018\)](#), for details

on the procedure. The 3σ -clipped mean differences of the proper motion along each direction ($\mu_\alpha \cos \delta$ and μ_δ) are considered as the best estimate of the zero points of the motions and are used to convert relative proper motions into absolute ones.

2.6 Calibration

In order to have a physical meaning, instrumental magnitudes need to be calibrated. The calibrated magnitude is given by the relation:

$$m_{cal} = m_{instr} + \Delta mag + ZP_{filt} + C$$

where m_{instr} is the instrumental magnitude, Δmag is the difference between PSF and aperture photometry, ZP_{filt} is the zero-point for a given filter and C is the aperture correction. In order to find Δmag , the routine **drz_phot_gfortran** has been used. It measures the aperture magnitudes in the images in .drz format, which are images of Bootes I at an exposure time of 1 s, thus with the values registered in each pixel that are actually the number of counts per unit second. It needs the following arguments: isolation index (HMIN), minimum and maximum flux (respectively FMIN and PMAX), and the image analyzed. The arguments are defined with the aim of considering only bright, isolated and not saturated stars. In order to perform the aperture photometry, the aperture radius, inner and outer radius has been defined. They have been chosen to be as large as possible, without including the flux of other nearby sources. The aperture magnitudes are then utilized to estimate Δmag . The procedure is iterative: plotting Δmag vs m_{instr} (obtained from PSF photometry) and considering the brightest and better-measured stars, one can find an average value of Δmag . In the first iteration, an initial by-eye value of Δmag and an interval around it of 4-5 σ (also this one imposed arbitrarily) have been used to select an initial sample of stars. Then, the Δmag median and the σ of the selected stars are calculated. Using these values as the initial ones, the procedure is repeated considering stars within an interval of 2-3 σ , until the result does not change between two subsequent iterations. The final result of these iterations is shown in [Figura]. The values of ZP_{filt} and C can be found from the utility available at <http://www.stsci.edu/hst/instrumentation/wfc3/calibration> for observation with WFC3 and at <http://www.stsci.edu/hst/acs/analysis/zeropoints> for observations in ACS. These values depend on the filter considered, the date of observation and the aperture radius.

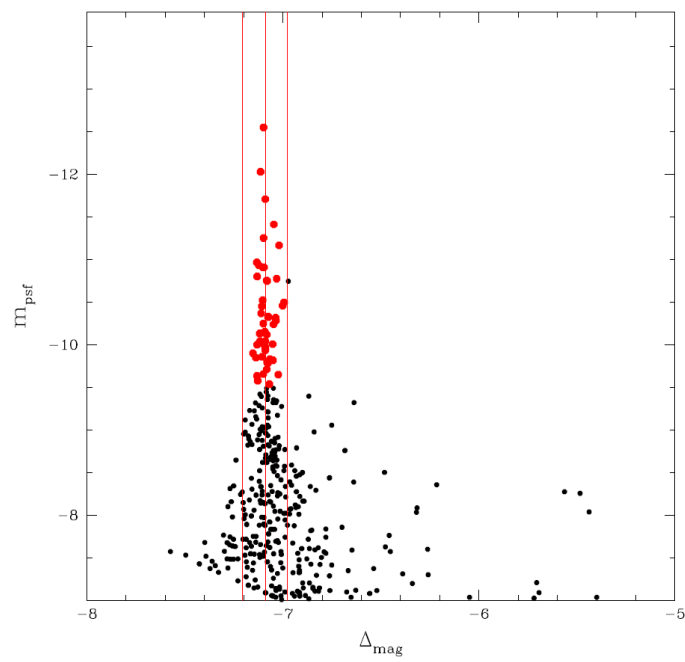


Figure 2.7: Plot of the instrumental magnitude (from PSF photometry) with respect to Δ_{mag} , used to find the latter one. The red vertical continuous line indicates the value of Δ_{mag} found from the iterative procedure and the dashed are located at a distance 3σ from the central one. The blue stars are the ones used to estimate the median.

Chapter 3

Data Analysis

This chapter analyzes the main outcomes of the investigation of the *HST* images and GAIA DR3 catalogs of Bootes I. It is organized as follows: in Section 3.1, I analyze the CMDs of the Bootes I members that I identify based on the relative proper motions. Section 3.2 is focused on the CMDs and the proper motions obtained by combining GAIA DR3 and *HST* data, while the orbit of Bootes I is presented in Section 3.3.

3.1 HST Color Magnitude Diagram and relative proper motion.

Figure 3.1 shows the CMD of stars in the field of view of Bootes I that I derived in Section 2.4. This CMD is derived from the images collected in 2019 alone, which provide the best photometry, due to the longest total exposure time.

What I want to do now, is to exclude in the best possible way the stars that do not belong to Bootes I, following the procedure described in section 2.5.2. It is important and necessary to have data from two different epochs, because stars will be in different positions in the sky, and this allows us to define the distance covered in that specific period and so the proper motion of every single star.

The comparison between the position variations in the 2012 and 2019 catalogues is shown in Figure 3.2, where the Bootes I's stars form a cloud-centred at (0,0), and the stars not belonging to the stellar system are located away from the origin. I set by eye a circle that separates members and non-members, highlighted in red in the Figure 3.2.

In Figure 3.3 I show the CMD of Bootes I, where grey dots represent sources too faint to have high-precision photometry (with $m_{F814W} < -7$), red dots are the stars excluded by my proper motion selection and black dots are the UFD's members.

The 2012 and 2019 CMDs with the members-only are illustrated in the left and right panels of Figure 3.4.

A visual inspection of the two CMDs reveals that the 2019 CMD is characterized by a lower noise, and is, in general, narrower with respect to the 2012 CMD. Indeed, all evolutionary phases, i.e. main sequence, sub-giant branch and red-giant branch, are better better defined. Moreover, Blue straggler stars are visible in both CMDs.

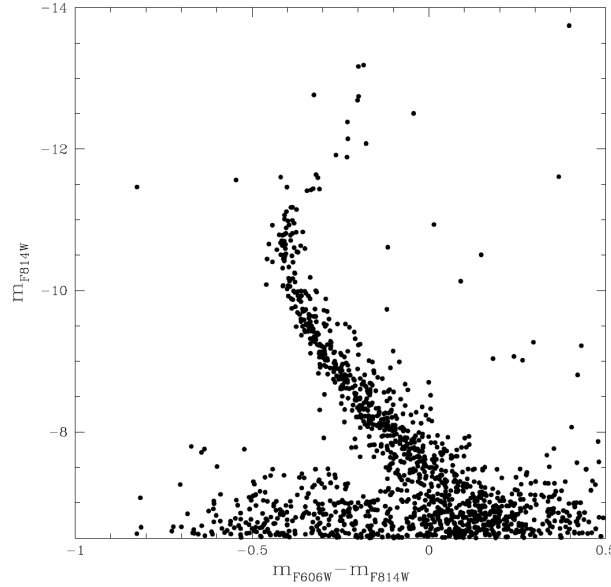


Figure 3.1: CMD of all stars in the field of view of Bootes I derived from 2019 data.

We can compare our result to the CMD of [Brown et al. \(2014\)](#) in Figure [1.7](#). They studied the Bootes I CMD applying the isochrone of M92 and estimating the age of the UFD. We can observe that in their case, as proper motions were not available, the CMD is strongly affected by noise and field stars contamination. For example, the blue stragglers, subgiant branch and red giant branch sequences are contaminated by non-members.

Finally, to calibrate the photometric catalog, I followed the procedure described in Section [2.5.2](#), Figure [3.5](#).

I fitted this CMD with isochrones to retrieve the age and metallicity of the UFD, exploiting the Dartmouth stellar evolution database [Dotter et al. \(2008\)](#). By deriving the best-fit isochrone, I obtained the following parameters: age = 13 Gyrs, metallicity $[Fe/H] = -2.4$, reddening $E(B-V) = 0.1$ and distance module = 18.45.

3.2 GAIA CMD

The data set of GAIA was built considering a radius of 5 arcmins, much bigger than the one of HST, covering a wider field of view but with less-accurate photometry, so that there is more background noise. Specifically, Gaia photometry covers only stars belonging to the sub-giant branch and brighter. This is the reason why stars observed by Gaia are saturated, increasing the errors but at the same time are the only ones that has been observed by Gaia and therefore the only common stars. Nonetheless, to convert HST relative proper motions into absolute ones, as described in [2.4](#), it is necessary to

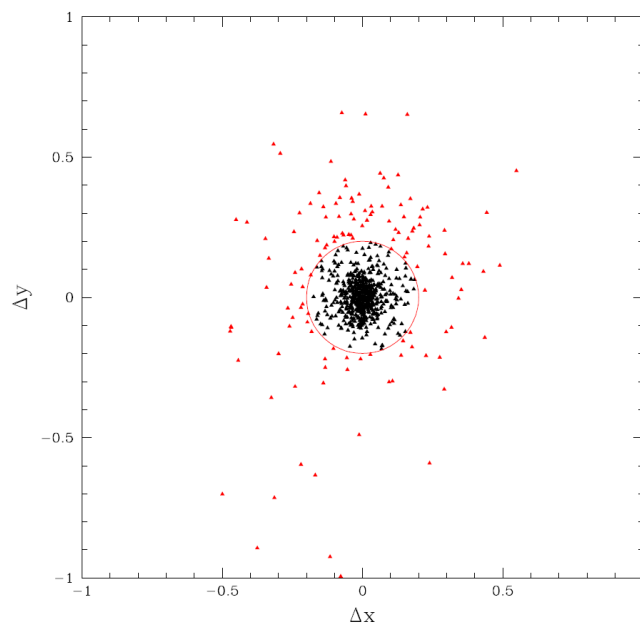


Figure 3.2: The proper motion of the stars. The blob of black stars in the central part, are all the stars that have a similar proper motion and so that belong to Bootes I, the red dot represents background and foreground stars that don't belong to the UFD.

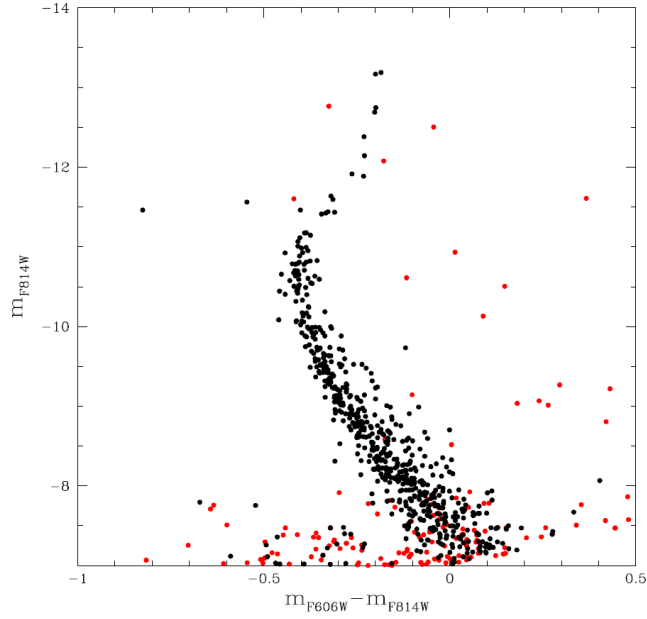


Figure 3.3: Black dots represent the stars that belong to Bootes I and so is the actual CMD, red dots are the background and foreground stars excluded because have different dispersion velocities with respect to Bootes I stars.

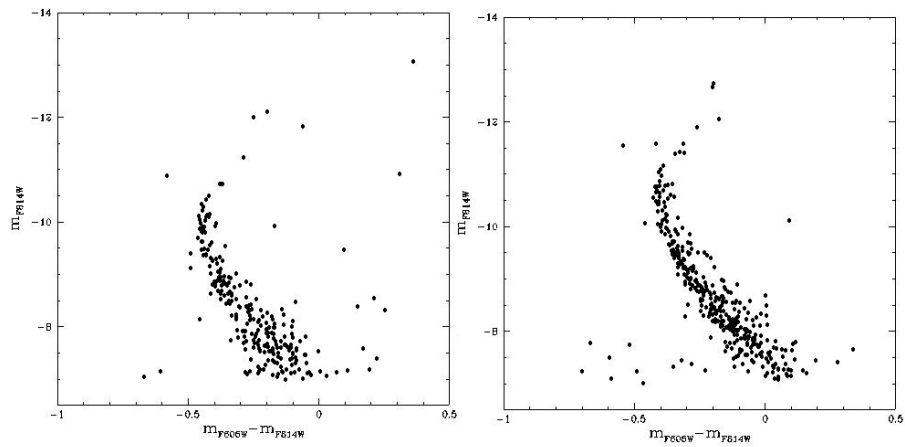


Figure 3.4: Comparison of the m_{F814W} vs. $m_{F606W} - m_{F814W}$ CMDs of stars in the field of Bootes I derived from 2012 (left) and 2019 (images).

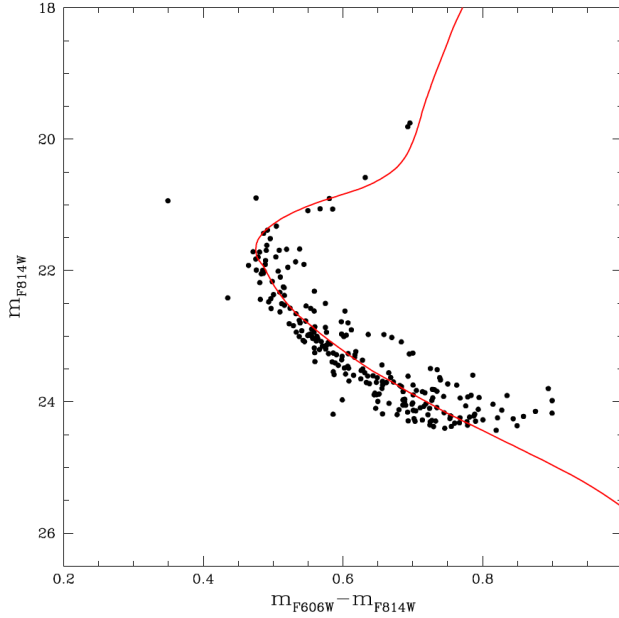


Figure 3.5: CMD of Bootes I after the calibration. Red dots represent the path of the isochrone.

exploit Gaia proper motions.

The comparison between the GAIA and HST datasets allows us to convert the relative proper motions into absolute ones. To identify UFD members in the GAIA catalogue, I consider two different ranges of the GAIA G_{rp} magnitude, namely between 20 and 11 and between 19 and 11, and compute the proper motions of stars within these intervals. While in the first range I have a larger number of stars, meaning higher statistics, in the latter case the sample includes brighter stars, translating into higher signal-to-noise ratio and therefore larger photometric accuracy.

I show in Figure 3.6 Figure 3.7 the GAIA proper motions (left panels) and the G_{rp} vs. $G_{bp} - G_{rp}$ CMDs (right panels) for the 20-to-11 and 19-to-11 magnitude ranges, respectively. In each plot, stars within the interval of interest are shown in black, while the ones outside are in grey. In the proper motion diagram, I defined a circle (in green) with a centre and radius given by the median and three times the dispersion (σ) of stars represented by black dots along both axes. Stars within the green circles are considered Bootes I members and are coloured in red in both Figures. The cleaned GAIA CMDs in these two ranges are represented in Figure 3.8 in the right and left panels.

Basically, the first range allows us to go down in magnitude and increase our set of common stars. The second case, with higher photometric accuracy, would be the best to take into consideration. However, due to the low number of stars detected by GAIA, it is better to consider the first case in which we have a larger number of stars.

In Figure 3.9 and Figure 3.10 I show the proper motions of the common stars

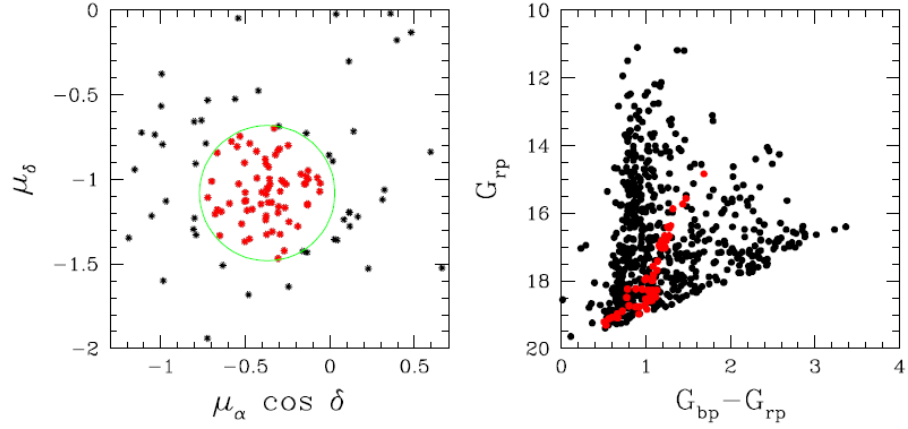


Figure 3.6: On the left, proper motions of the stars, in red are the stars that belong to Bootes I, black points are the background stars. On the right the CMD is presented, red stars are the CMD of Bootes I and in black are the background stars.

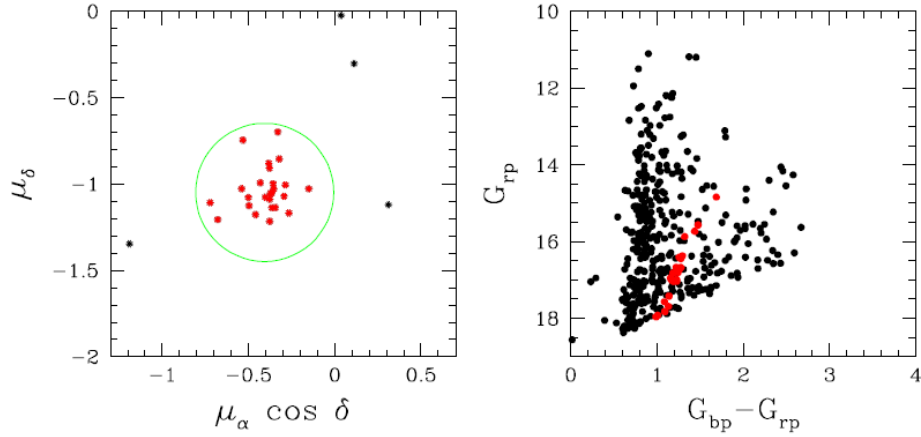


Figure 3.7: On the left, proper motions of the stars, in red are the stars that belong to Bootes I, and black points are the background stars. On the right the CMD is presented, red stars are the CMD of Bootes I and black are the background stars.

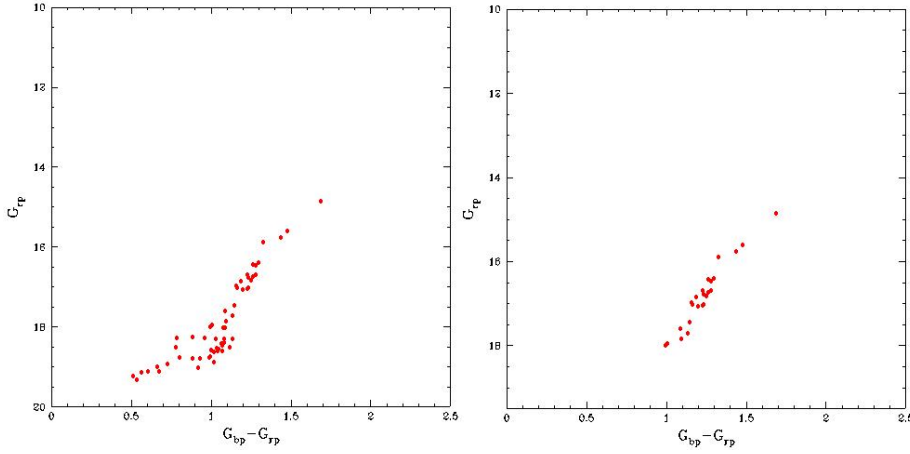


Figure 3.8: (On the right) CMD Bootes I by GAIA archive, only stars with magnitude in this range: $20 < m < 11$. (On the left) CMD Bootes I by GAIA archive only stars with magnitude in this range: $19 < m < 11$.

measured by HST as a function of the proper motion measured by Gaia. The fact that they sit on the diagonal allows us to say that are well correlated.

This study allows us to define the weighted average of the star's absolute proper motion. I will determine this value by taking into consideration two different stellar samples:

1. Accounting only for HST not saturated stars in common with Gaia, so in a range of magnitude $-7 < m_{F606W} < -13$. Figure 3.13
2. Accounting the full set of common stars, so also including saturated stars. Figure 3.14 represents the same quantities of Figure 3.13 but with this larger sample of stars.

I used Figure 3.11 and Figure 3.12 to do a preliminary cleaning of the stars which have a large error in the proper motion on x or y axis, to exclude outliers in the computation of the weighted average.

Once these stars are excluded, I can compute the weighted average of the GAIA proper motions in the two different cases:

1. The weighted average of the proper motions for the non-saturated stars are: $\mu_a \cos \delta_{wa} = 1.01 \pm 0.28$ mas/yr, and $\mu_{\delta_{wa}} = 1.21 \pm 0.28$ mas/yr. Figure 3.13
2. By considering all the stars, including the saturated ones, I obtain $\mu_a \cos \delta_{wa} = 0.38 \pm 0.24$ mas/yr, $\mu_{\delta_{wa}} = 1.25 \pm 0.26$ mas/yr. Figure 3.14

Red lines in both figures represent the weighted average of proper motions and green lines represent the error's range. The values inferred by including also the HST saturated stars are based on higher statistics and therefore are characterized by a lower error on the weighted average. The results obtained with the two approaches are consistent with

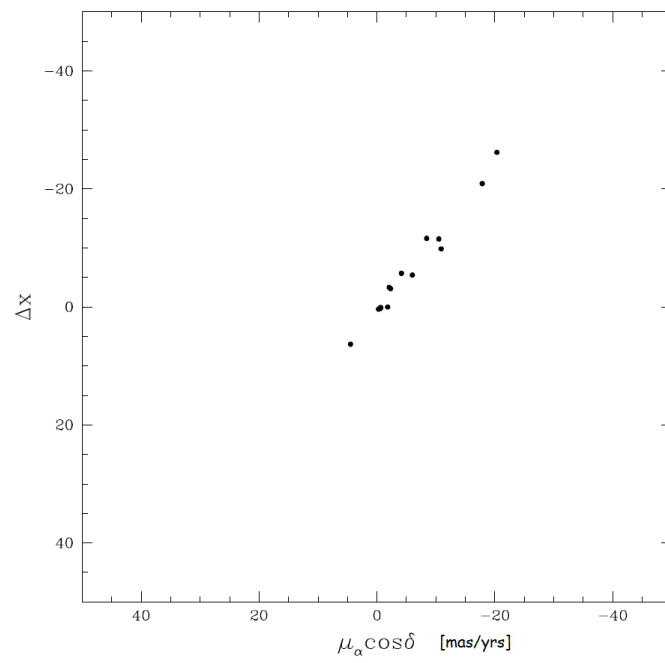


Figure 3.9: Comparison between the variation on the x-axis for each star, in this plot we compare the variation on this axis in the GAIA and HST study.

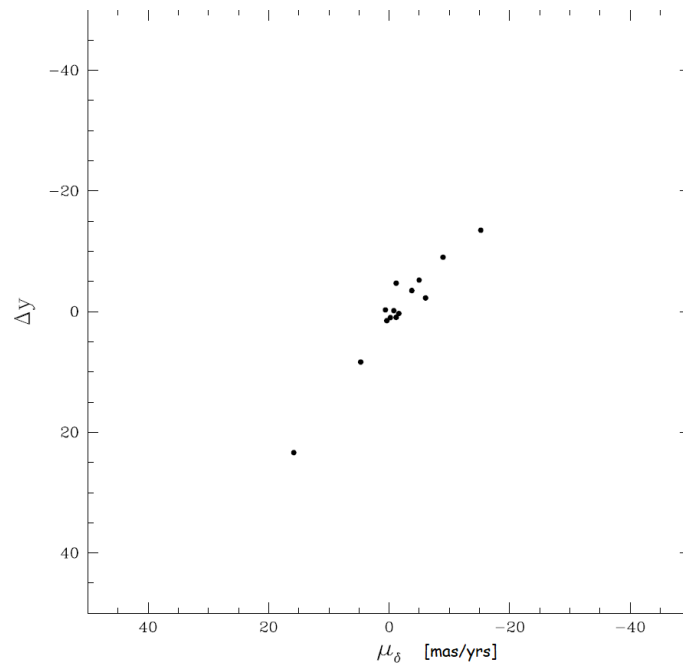


Figure 3.10: comparison between the variation on the y-axis for each star, in this plot we compare the variation on this axis in the GAIA and HST study.

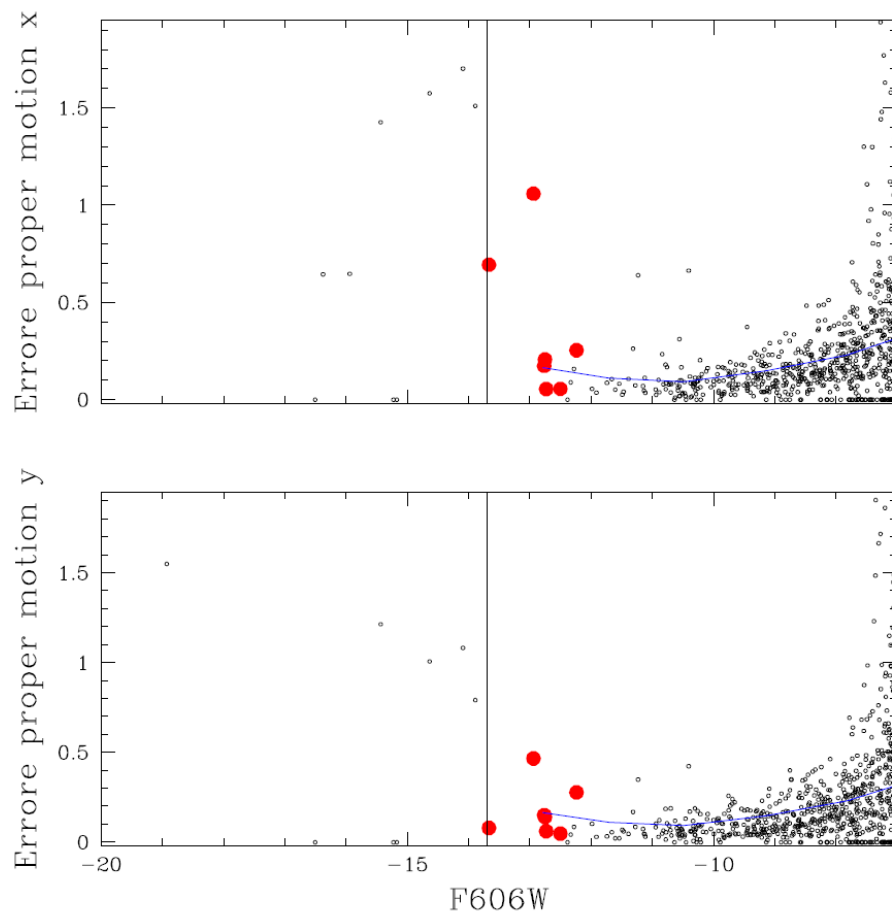


Figure 3.11: Top image: proper motion error on the y-axis, in the image below the proper motion error on the x-axis, against the magnitude in the filter F606W. . The red dots are the stars that have been excluded by our data set due to errors, that does not fit our interpolation. The blue fiducial line represents the median of the proper motion error that we expect for the star at a specific magnitude.

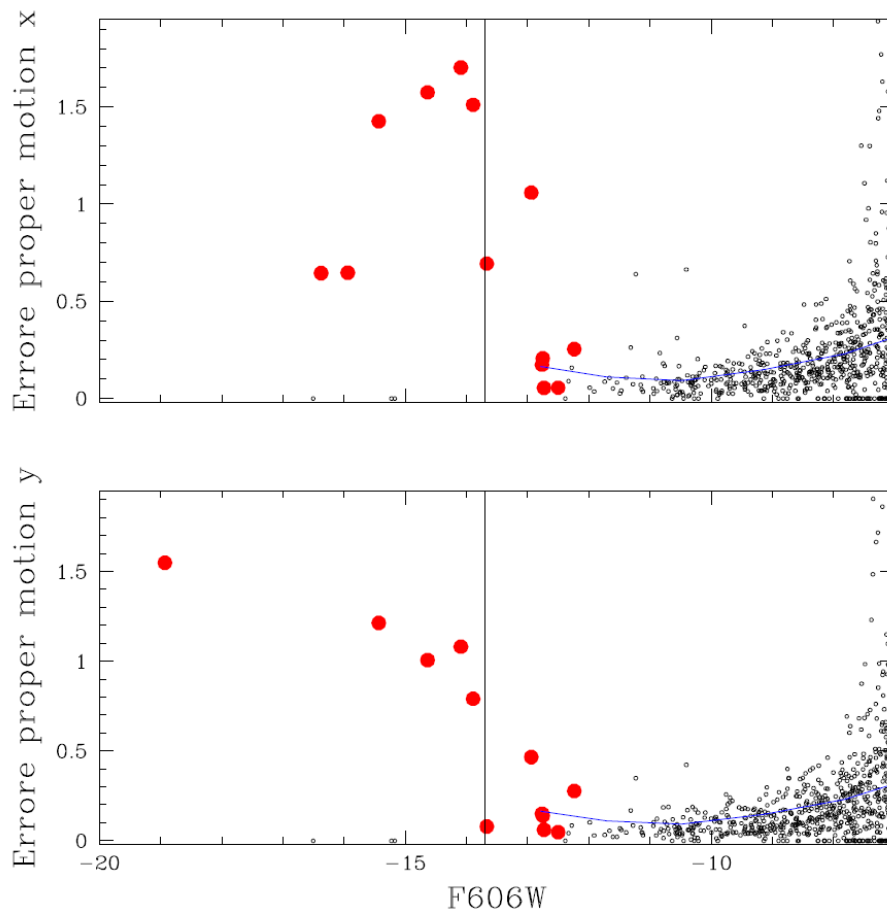


Figure 3.12: Top image: proper motion error on the y-axis, in the image below the proper motion error on the x-axis, against the magnitude in the filter F606W. Bot image: proper motion error on the y-axis, in the image below the proper motion error on the x-axis, against the magnitude in the filter F606W. The red dots are the stars that have been excluded by our data set due to errors, that do not fit our interpolation. The blue fiducial line represents the median of the proper motion error that we expect for the star at a specific magnitude.

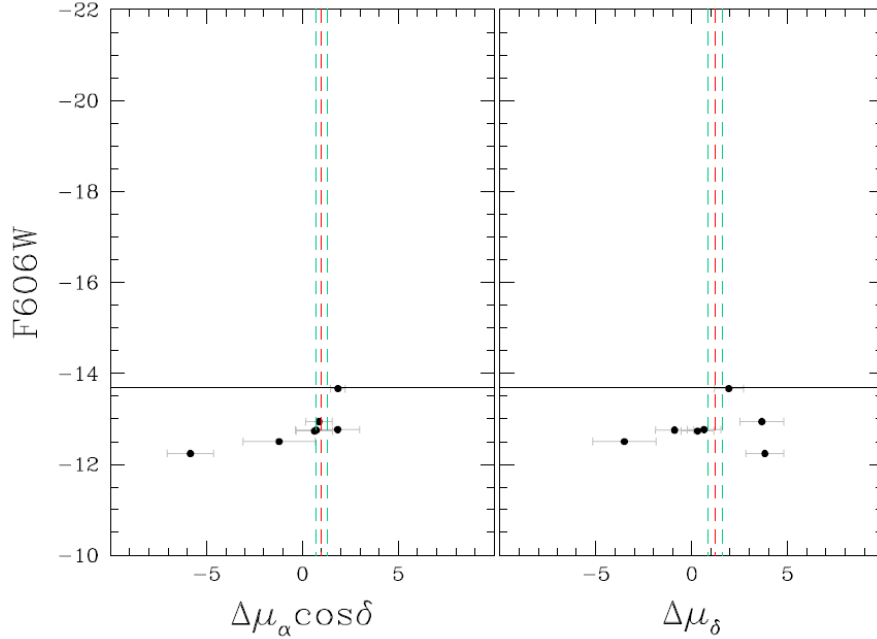


Figure 3.13: Black dots represent the common stars between Gaia and HST with the errors, with a limitation of only non-saturated stars, so with a $M_V < -13.7$. The red dot line represents the weighted average of the errors and the green lines represent the error range.

each other on the μ_δ , while I observe that along the x-axis the weighted average is significantly smaller in the second case.

3.3 Bootes I Orbit

To compute the orbit of Bootes I the full 6-dimensional information on the position and velocity is needed. In particular, we need right ascension (α), declination (δ), distance from the Sun (d), proper motions in right ascension and declination ($\mu_\alpha \cos \delta$, μ_δ) and the heliocentric radial velocity (v_r). Once the full position and velocity are known, the kinematics of the object can be determined using the GALPY public Python package (Bovy, 2015).

Specifically, we adopted the potential identified as the best candidate among the ones studied in McMillan (2017), which consists of an axisymmetric model with a bulge, thin, thick, and gaseous disks and a Navarro-Frenk-White (Navarro et al., 1996) dark matter halo. Finally, after directly integrating the orbit of Bootes I 4 Gyr backwards and forward in time, using the following values for the position and velocity:

- distance from the Galactic Centre (GC) is taken from Belokurov et al. (2006) and

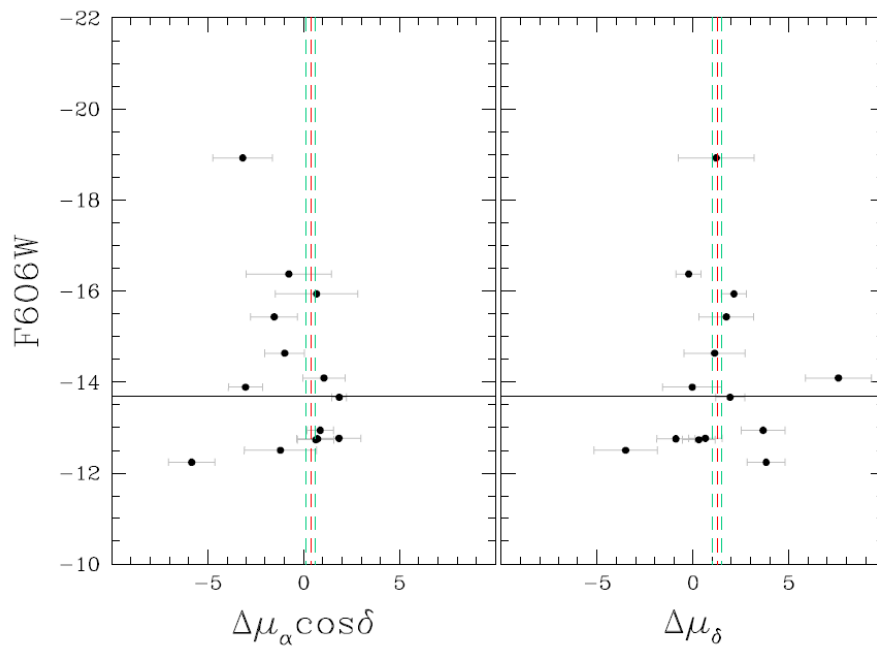


Figure 3.14: Black dots represent the common stars between Gaia and HST with the errors, with no limitation on the magnitude, taking the saturated one, and so with a $M_V < -22$. The red dot line represents the weighted average of the errors and the green lines represent the error range.

corresponds to 66.2 ± 6.0 kpc

- radial velocity $v_r = 101.8 \pm 0.7$ km/s from [Norris et al. \(2009\)](#)
- $\alpha = 210.023 \pm 0.015$ and $\delta = 14.501 \pm 0.015$ ([Brown et al., 2014](#))
- $\mu_\alpha \cos \delta = 0.38 \pm 0.24$ and $\mu_\delta = 1.25 \pm 0.26$

The uncertainties associated with the derived orbital parameters are determined by sampling the Probability Distribution Functions (PDFs) of the observed values. In particular, we drew 500 random realizations of the 3-dimensional position and velocity components and, for each realization, recomputed the orbital parameters assuming Gaussian distributions with means and dispersions equal to the observed values and their uncertainties. In particular, the uncertainties in the two proper motion components ($\mu_\alpha \cos \delta$, μ_δ) have been drawn from a bivariate Gaussian.

The output is an orbit with eccentricity $e = 0.4 \pm 0.2$, perigalactic distance $D_{peri} = 27.1 \pm 15.4$, apocentric distance $D_{apo} = 67.2 \pm 3.7$, and maximum vertical excursion from the Galactic plane $|Z_{max}| = 66.5 \pm 3.5$ kpc. This orbit is displayed in the bottom panels of [Figure 4.1](#) where each point is colour-coded according to the integration time, as defined in the right color bar. Moreover, we re-computed the orbit of Bootes I adopting the literature values for the proper motion components, instead of the ones derived in the present work, changing only the values of the proper motion $\mu_\alpha \cos \delta = 0.39 \pm 0.02$ and $\mu_\delta = 1.06 \pm 0.01$ ([Battaglia et al., 2022](#)). The resulting orbit is shown in the upper panels of [Figure 4.1](#). Clearly, a visual inspection of [Figure 4.1](#) reveals that the two orbits are consistent with each other, with small differences between their orbital properties.

Other important values are $U = 191.5$ km/s (motion on the galactic plane), $V = -366.7$ km/s (perpendicular to U), and on the direction orthogonal to the galactic plane $W = 44.2$ km/s.

Chapter 4

Discussion and conclusions

In this thesis, I analyzed the UFD Bootes I. Thanks to the high quality of the photometry provided by HST and GAIA, it is possible to resolve its stars and obtain detailed information about the nature of this object. To do that, I reduced archive HST images taken in two different epochs using state-of-the-art techniques to perform high-precision photometry. The main results of my thesis are here summarized:

1. By exploiting my multi-epochs dataset, I compared the 2012 and 2019 observations to determine the proper motions of stars within the observed field. This allowed me to exclude, with great accuracy, field stars which are not members of the UFD, thus improving the CMD of Bootes I, with respect to previous works (e.g. [Brooks & Zolotov \(2014\)](#), [Filion et al. \(2022\)](#)).
2. By using GAIA DR3 observations and comparing them with the HST catalog, I was able to compute the absolute proper motion of Bootes I, obtaining: $\mu_{\alpha\cos\delta} = 0.38 \pm 0.24$, and the $\mu_{\delta} = 1.25 \pm 0.26$. [Battaglia et al. \(2022\)](#) measured the same quantities by using Gaia observations only and assessing the UFD membership exploiting a maximum likelihood approach (see their paper for details). Battaglia and collaborators found on $\mu_{\alpha\cos\delta} = 0.39 \pm 0.02$ and on $\mu_{\delta} = 1.06 \pm 0.01$. While the first value is in exquisite accord with my result, the latter is slightly higher, but still consistent with errors.
3. Using my results on the absolute proper motion, I was also able to compute the orbit of Bootes I, whose orbital parameters are reported in Figure [4.1](#).

Actually, we have taken into consideration only about nine of the HST quadrant, going on doing this kind of study for every remaining quadrant we can improve the quality and the accuracy of every computation. My results provide a further characterization of the Bootes I stellar population and its kinematic, based on the synergy between HST and GAIA photometry, which constitutes a solid approach to shed light on the kinematics of MW satellite galaxies, such as the UFD here analyzed. Future analysis, extending the sample to other similar objects, is crucial to retrieve new insights into the characteristics of small satellites that populate the surrounding of our galaxy.

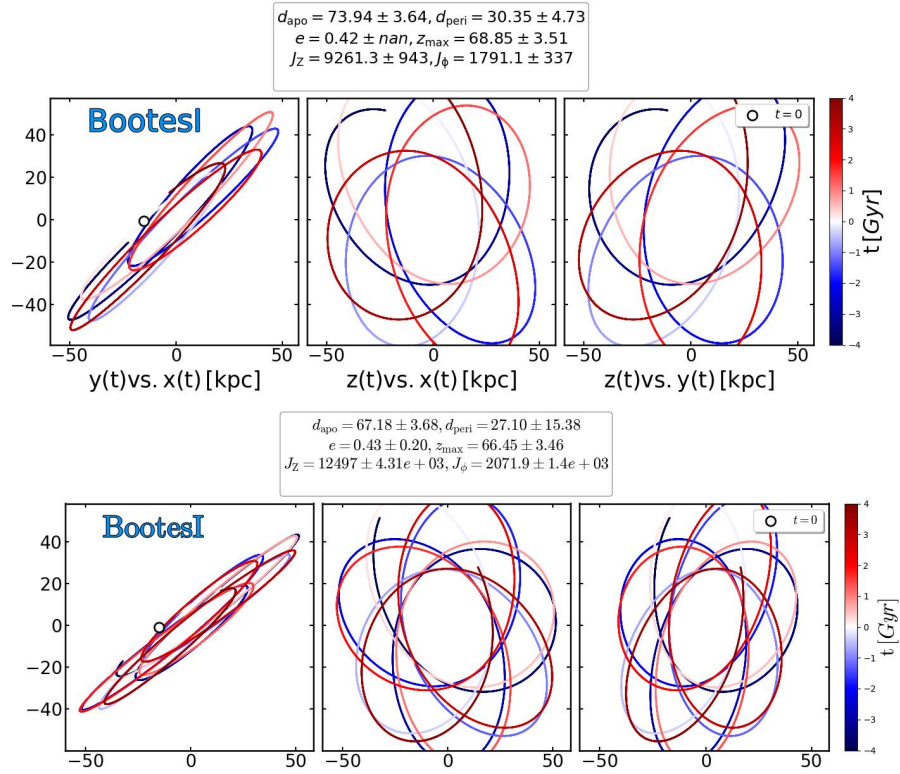


Figure 4.1: Upper image: Orbit computed with the 6d information derived in literature works. Bottom image: The integrated orbit of the UFD Boots I over a period of 4 Gyr, backward and forward in time. Color coding is described by the right colorbar, while the white thick dot indicates the present-day position of Boots I.

Table 4.1: Magnitude and shift of common stars between Gaia and HST

F606W	F814W	Variation in RA	variation in DEC
-15.22	-15.89	5.50	-30.94
-15.17	-16.19	-24.28	-22.99
-12.73	-13.09	-6.01	-3.78
-16.37	-16.13	-2.31	-4.98
-12.38	-13.74	0.37	-36.25
-15.43	-15.26	-4.15	-15.21
-14.09	-15	-10.89	15.91
-12.75	-12.52	-0.62	0.61
-12.76	-12.55	-1.81	-0.79
-15.94	-15.9	-0.27	-1.17
-12.23	-13.38	-20.35	-6.1
-12.5	-12.13	-2.08	-1.17
-16.5	-16.36	-13.19	-43.92
-13.67	-13.99	4.485	-1.6
-14.63	-14.3	-10.51	0.38
-18.93	-18.58	-8.43	-0.2
-12.94	-14.21	-0.61	4.72
-13.89	-13.87	-17.85	-8.95

Bibliography

- Anderson J., King I. R., 2000, [PASP](#), [112](#), 1360
- Battaglia G., Taibi S., Thomas G. F., Fritz T. K., 2022, [A&A](#), [657](#), A54
- Bechtol K., et al., 2015, [ApJ](#), [807](#), 50
- Bedin L. R., Piotto G., Anderson J., King I. R., 2003, in Piotto G., Meylan G., Djorgovski S. G., Riello M., eds, *Astronomical Society of the Pacific Conference Series Vol. 296, New Horizons in Globular Cluster Astronomy*. p. 360 ([arXiv:astro-ph/0303291](#))
- Belokurov V., et al., 2006, [ApJ](#), [647](#), L111
- Belokurov V., et al., 2007, [ApJ](#), [658](#), 337
- Boselli A., Boissier S., Cortese L., Gavazzi G., 2008, [A&A](#), [489](#), 1015
- Bovy J., 2015, [ApJS](#), [216](#), 29
- Brooks A. M., Zolotov A., 2014, [ApJ](#), [786](#), 87
- Brown T. M., et al., 2012, [ApJ](#), [753](#), L21
- Brown T. M., et al., 2014, [ApJ](#), [796](#), 91
- Clem J. L., Vanden Berg D. A., Stetson P. B., 2008, [AJ](#), [135](#), 682
- Cole A. A., et al., 2007, [ApJ](#), [659](#), L17
- Cordoni G., Milone A. P., Marino A. F., Di Criscienzo M., D'Antona F., Dotter A., Lagioia E. P., Tailo M., 2018, [ApJ](#), [869](#), 139
- Cordoni G., Milone A. P., Mastrobuono-Battisti A., Marino A. F., Lagioia E. P., Tailo M., Baumgardt H., Hilker M., 2020, [ApJ](#), [889](#), 18
- Dall'Ora M., et al., 2006, [ApJ](#), [653](#), L109
- Di Cintio A., Brook C. B., Macciò A. V., Stinson G. S., Knebe A., Dutton A. A., Wadsley J., 2014, [MNRAS](#), [437](#), 415
- Dotter A., Chaboyer B., Jevremović D., Kostov V., Baron E., Ferguson J. W., 2008, [ApJS](#), [178](#), 89

- Drlica-Wagner A., et al., 2015, [ApJ](#), [813](#), [109](#)
- Ellis R. S., 1997, [ARA&A](#), [35](#), [389](#)
- Filion C., Platais I., Wyse R. F. G., Kozhurina-Platais V., 2022, [ApJ](#), [939](#), [38](#)
- Freeman K. C., 1970, [ApJ](#), [160](#), [811](#)
- Gallart C., Monelli M., Dolphin A., Bernard E., Drozdovsky I., Aparicio A., Cassisi S., 2007, in Vallenari A., Tantalò R., Portinari L., Moretti A., eds, *Astronomical Society of the Pacific Conference Series Vol. 374, From Stars to Galaxies: Building the Pieces to Build Up the Universe*. p. 253
- Geha M., et al., 2013, [ApJ](#), [771](#), [29](#)
- Hidalgo S., Aparicio A., Gallart C., Monelli M., Stetson P. B., Walker A. R., 2011, *Toward a detailed, reliable and comprehensive star formation history of the Small Magellanic Cloud*, NOAO Proposal ID 2011B-0051
- Hodge P. W., 1971, [ARA&A](#), [9](#), [35](#)
- Hughes J., Wallerstein G., Bossi A., 2008, [AJ](#), [136](#), [2321](#)
- Jones J. B., Phillipps S., Schwartzberg J. M., Parker Q. A., 1998, arXiv e-prints, [pp astro-ph/9805287](#)
- Kirby E. N., Simon J. D., Geha M., Guhathakurta P., Frebel A., 2008, [ApJ](#), [685](#), [L43](#)
- Kirby E. N., Cohen J. G., Guhathakurta P., Cheng L., Bullock J. S., Gallazzi A., 2013, [ApJ](#), [779](#), [102](#)
- Kleyna J. T., Wilkinson M. I., Evans N. W., Gilmore G., 2005, [ApJ](#), [630](#), [L141](#)
- Koposov S. E., et al., 2011, [ApJ](#), [736](#), [146](#)
- Koposov S. E., et al., 2018, [MNRAS](#), [479](#), [5343](#)
- Kormendy J., 1985, [ApJ](#), [295](#), [73](#)
- Martin N. F., Ibata R. A., Chapman S. C., Irwin M., Lewis G. F., 2007, [MNRAS](#), [380](#), [281](#)
- Martin N. F., de Jong J. T. A., Rix H.-W., 2008, [ApJ](#), [684](#), [1075](#)
- Marzke R. O., da Costa L. N., 1997, [AJ](#), [113](#), [185](#)
- Mateo M. L., 1998, [ARA&A](#), [36](#), [435](#)
- McConnachie A. W., Côté P., 2010, [ApJ](#), [722](#), [L209](#)
- Milone A. P., Villanova S., Bedin L. R., Piotto G., Carraro G., Anderson J., King I. R., Zaggia S., 2006, [A&A](#), [456](#), [517](#)

- Muñoz R. R., Carlin J. L., Frinchaboy P. M., Nidever D. L., Majewski S. R., Patterson R. J., 2006, [ApJ](#), **650**, L51
- Muñoz R. R., Geha M., Willman B., 2010, [AJ](#), **140**, 138
- Muñoz R. R., Côté P., Santana F. A., Geha M., Simon J. D., Oyarzún G. A., Stetson P. B., Djorgovski S. G., 2018, [ApJ](#), **860**, 66
- Navarro J. F., Frenk C. S., White S. D. M., 1996, [ApJ](#), **462**, 563
- Norris J. E., Gilmore G., Wyse R. F. G., Wilkinson M. I., Belokurov V., Evans N. W., Zucker D. B., 2008, [ApJ](#), **689**, L113
- Norris J. E., Gilmore G., Wyse R. F. G., Wilkinson M. I., Belokurov V., Evans N. W., Zucker D. B., 2009, [ApJ](#), **695**, L217
- Norris J. E., Yong D., Gilmore G., Wyse R. F. G., 2010a, [ApJ](#), **711**, 350
- Norris J. E., Wyse R. F. G., Gilmore G., Yong D., Frebel A., Wilkinson M. I., Belokurov V., Zucker D. B., 2010b, [ApJ](#), **723**, 1632
- Oñorbe J., Boylan-Kolchin M., Bullock J. S., Hopkins P. F., Kereš D., Faucher-Giguère C.-A., Quataert E., Murray N., 2015, [MNRAS](#), **454**, 2092
- Peñarrubia J., Ludlow A. D., Chanamé J., Walker M. G., 2016, [MNRAS](#), **461**, L72
- Piotto G., et al., 2012, [ApJ](#), **760**, 39
- Ryan-Weber E. V., Begum A., Oosterloo T., Pal S., Irwin M. J., Belokurov V., Evans N. W., Zucker D. B., 2008, [MNRAS](#), **384**, 535
- Siegel M. H., 2006, [ApJ](#), **649**, L83
- Simon J. D., Geha M., 2007, [ApJ](#), **670**, 313
- Tammann G. A., 1994, in European Southern Observatory Conference and Workshop Proceedings. p. 3
- Torrealba G., Kopsosov S. E., Belokurov V., Irwin M., 2016, [MNRAS](#), **459**, 2370
- Tremonti C. A., et al., 2004, [ApJ](#), **613**, 898
- Unavane M., Wyse R. F. G., Gilmore G., 1996, [MNRAS](#), **278**, 727
- Weisz D. R., Dolphin A. E., Skillman E. D., Holtzman J., Gilbert K. M., Dalcanton J. J., Williams B. F., 2014, [ApJ](#), **789**, 147
- Whiting A. B., Irwin M. J., Hau G. K. T., 1997, [AJ](#), **114**, 996
- Willman B., et al., 2005, [AJ](#), **129**, 2692
- Wolf J., Martinez G. D., Bullock J. S., Kaplinghat M., Geha M., Muñoz R. R., Simon J. D., Avedo F. F., 2010, [MNRAS](#), **406**, 1220
- de Jong J. T. A., et al., 2008, [ApJ](#), **680**, 1112